Restructuring in high burn-up PWR UO_2 fuel central parts: experimental 3D characterization by focused ion beam – scanning electron microscopy

Jean Noirot[1], Rébecca Dowek[1, 2], Isabelle Zacharie-Aubrun[1], Thierry Blay[1], Martiane Cabié[3], Myriam Dumont[4]

[1] *CEA, DES, IRESNE, DEC, Cadarache F-13108 Saint-Paul-Lez-Durance, France, jean.noirot@cea.fr*
[2] Aix-Marseille University, Institut Matériaux Microélectronique Nanosciences de Provence-IM2NP, UMR CNRS 7334, France
[3] *Aix Marseille Univ., CNRS, FSCM, CP2M, France*
[4] *Arts et Métiers Institute of Technology, MSMP, HESAM Université, F-59000 Lille, France*

Abstract

FIB-SEM 3D examination was conducted on three standard UO_2 and one Cr doped UO_2 high burn-up PWR fuel samples. This work complemented other microanalysis examination, including an EBSD work on the polished surface. A parallel article giving the EBSD results was submitted simultaneously. Together, they found, in all the central area of these high burn-up samples:

- a restructuring of the initial grains into smaller sub-grains forming low angle boundaries and with crystal orientations around that of their parent grains,
- intragranular bubbles mostly situated on these low angle boundaries.

The FIB-SEM 3D examination showed how such inter-sub-grain bubbles start as small compact but also small lenticular bubbles, similar to typical small intergranular lenticular bubbles. With increasing burn-up, these lenticular bubbles get thicker and locally interlink to form more complex bubbles. However, no long distance networks, between the sub-grains, or between the original grains, were found. Such networks could have been a path for part of the fission gases to reach the grain boundaries, the grain edges (the intersection line of three grain boundaries) and the rod free volumes. These FIB-SEM 3D examinations brought details on the intragranular and intergranular bubbles situation for each studied volume. Distribution of the intragranular bubbles according to their sizes and shapes were exposed. The central restructuring, studied in this work, is likely to play a role in the increase of the fission gas release fractions at high burn-up. This work is an incentive to study further this restructuring and the bubbles formed, combining different approaches.

1. Introduction

Nuclear fuels are submitted, during their use in nuclear reactors, to a number of damage sources. The main ones are the neutrons, with a wide range of energies, β and α decay and their direct consequences, including heavy atom recoils, but above all, the fission products, transferring their energies through electronic interaction and nuclear interaction. The progress in the use of the fuel is generally monitored by its burn-up. It is expressed as the fraction of initial heavy atoms that have fissionned (at% or %FIMA, Fissions per Initial Metal Atom) or by the energy generated per unit mass of initial heavy metal (GWd/t_{HM}) or, for uranium based fuels (GWd/t_U). In addition to the point defects and extended defects, induced by the various damage sources, the composition of the fuel evolves. This is due to the fissions of heavy atoms, forming fission products, to the transmutation of heavy atoms and of fission products by neutron captures, and to the various radioactive decays. Table 1 gives an idea of the composition change reached in a PWR UO_2 at high burn-up.

	U	Ra + other actinides	Fission Products
fabrication	**100%**	**0%**	**0%**
At 60 GWd/t_U	**86.9%**	**1.3%**	**11.7%**

Table 1: Typical composition changes in the UO_2 at high burn-up. The fractions are atomic fractions and oxygen is not considered.

All this induces changes in the fuel mechanical and thermal properties. Nevertheless UO_2 and $(U,Pu)O_2$ keep their crystal structure, exhibiting a very high resistance to irradiation.

Among the fission products there are gases, xenon and krypton. They account for about 15% of the fission products. They are not soluble in the UO_2 or $(U,Pu)O_2$ and tend to form bubbles. These bubbles can be intragranular (inside the grains) or intergranular (along grain boundaries or grain edges i.e. the intersection line between three grain boundaries). The size of these bubbles tends to increase with the fuel temperatures. In the PWR fuels, below ~40 GWd/t_U these bubbles generally remain small, necessitating transmission electron microscopy to characterize them [1-3]. Nevertheless, in case of high linear powers, such as those reached in dedicated tests in material testing reactors, with linear powers typically higher than ~300 W/cm, or after annealing of irradiated fuels in high activity laboratories, with temperatures typically higher than 1200°C, much larger bubbles are found. Reaching micrometric sizes such bubbles are visible with scanning electron microscopes (SEM) and optical microscopes [2,4-11].

At higher burn-up however, there are bubbles detectable with optical microscopy even in rods where the central temperature never exceeded 900°C and was below 800°C at the end of the irradiation.

In UO_2 fuels, this is the case on the rim of the pellets, where a massive restructuring of the original grains occurs. In this restructuring, called HBS (High Burn-up Structure) the original grains, with typical diameters around 10 µm, are replaced by thousands of smaller grains with typical diameters around 0.5 µm. In this process, most of the fission gas leaves the grains and forms large micrometric intergranular bubbles. This phenomenon was extensively studied during the last three decades and is still being studied [12-24], all the more that this part of the fuel is prone to fragmentation in loss of coolant accident situations (LOCA) [25-29].

In the same range of burn-up for which the HBS forms on the rim of the Light water reactor (LWR) UO_2 fuel pellets, micrometric or sub-micrometric fission gas bubbles also form in a central area of the pellets [30]. This phenomenon was generally attributed to the combined effect of the temperatures being the highest in the pellets, and of the increasing fission gas build-up. In the studies at high linear powers, and lower burn-ups, such central porous areas were commonly found [31]. This formation of bubbles in the center at high burn-up, without high linear powers, was therefore not studied as much as the HBS phenomenon. In [32], in 2004, we showed that in these central areas at high burn-up, the grain contrasts due to electron channeling differences on SEM images did not allow separating the grains, for sample preparations for which this was possible outside the central area. In [33], in 2009, in the center of a 73 GWd/t_U SEM fractography, no easy identification of the grain boundaries was possible and the bubbles were neither spherical (as typical intragranular bubbles), nor clearly lenticular (as typical intergranular bubbles before interconnection), and they did not seem to be widely interconnected. The first questions raised by these observations were addressed in [34], in 2018, combining 3D focused ion beam (FIB-SEM) examinations and electron back scattered diffraction (EBSD) on the 73 GWd/t_U fuel. These techniques showed the formation of low angle boundary sub-grains within the initial grains (called subdomains in [34]). These sub-grains have crystal orientations close to those of their respective parent grains. Similar observations and measurements of central grain restructuring were published by Gerczak et al. in [24] on a 72 GWd/t_U UO_2 fuel. Such grain restructuring was also observed in Al-Si and Al-Cr doped fuels, by Jädernäs et al. in [35]. Very recently, Cappia et al. [36] reported similar restructuring in a 76 GWd/t_U PWR UO_2 fuel section.

In addition to the sub-grain formations, in [34] the FIB-SEM examinations showed the presence of inter-sub-grain bubbles, with complex shapes, and the absence of an interconnected bubble network.

After [34], the only FIB-SEM 3D study published on an irradiated high burn-up LWR fuel, to the authors' knowledge, was that of McKinney et al. [37]. In this work, the FIB-SEM technique was applied on the same sample already examined by Gerczak et al. [24], with EBSD, 2D SEM with Energy Dispersive X-ray Spectroscopy (EDS) and with transmission Kikuchi diffraction (tKD). This sample was a short longitudinal cut of a UO_2 specimen with a local burn-up of 72 GWd/t_U covering ~0.23R – 1R (where R is the pellet's radius, 1R its periphery and 0R its center –convention that will be used all through this article). This fuel was a 2.9% ^{235}U fuel with a pellet diameter of 9.06 mm before irradiation. It was part of an experimental program and irradiated in H.B. Robinson Unit 2 PWR. The linear power for the central region of the rod showed a general decrease from ~260 W/cm to ~120 W/cm. The rod fission gas release at the end of the irradiation was 2.1% of the production. In this FIB-SEM work, SEM images had pixels of 4.56 nm in both directions but the space between these SEM images were of 55 to 63 nm. The bubbles were characterized based on their size, shape, number density, and percentage of the total volume they occupied. The shapes were classified into four classes: spheroids, for which the bubbles had similar principal axis lengths, footballs (American football) for which the bubbles had two similar principal axis lengths but one clearly longer than the others, disks, for which the bubbles had two similar principal axis lengths but one clearly shorter than the others, and "others" for bubbles for which the similarity threshold of 50% was passed. In the HBS region, no interconnection that could facilitate fission gas release was observed. At ~0.24R, consistently with the observations in [34], despite the presence of large and complex bubbles, there were still no observed large interconnected networks like those needed for fission gas release pathways.

For these new results, partly produced during the PhD work of R. Dowek, the FIB-SEM technique was applied to four PWR fuel samples: three standard UO_2 and one Cr doped UO_2. The standard UO_2 fuels had grain sizes around 9 µm and average cross section burn-ups between 61 GWd/t_U and 73 GWd/t_U. The Cr doped UO_2 had grain sizes around 60 µm and a cross section burn-up of 63 GWd/t_U. This article focuses on the bubbles formed at high burn-up in the central parts of the pellets without particularly high irradiation powers. A parallel article [38] exposes the results of the EBSD examination technique applied to selected areas at various radial positions on the polished surface of the same cross sections. This EBSD work was also extended to lower burn-up samples for which 3D FIB-SEM characterization was less interesting, considering the low fission gas bubble formation.

In this article, section 2 provides information on the studied samples, describes the devices used and the main data processing steps and explains the principles used to separate the fission gas bubbles into classes according to shape indicators. Section 3.1 gives and comments one 2D image from the 3D stacks, for each sample and radial position. Section 3.2 shows details of intragranular bubbles for each radial position and for each sample. Section 3.3 shows details on intergranular bubbles for each radial position and for each sample. In these sections 3.2 and 3.3, 3D reconstruction views on these detailed volumes are provided. In section 4, the shape classification described in section 2.3 is applied to all the studied volumes in the central areas, with views of the 3D reconstructions and quantitative distributions derived from these reconstructions. These results are further discussed and compared with some of the corresponding EBSD results of [38] in section 5.

2. Specimens, examination devices and shape classes

2.1 Specimen studied

The specimens, studied by 3D FIB-SEM examinations, and used in this work, were all PWR irradiated UO_2 fuel entire cross sections. They were embedded in a low melting point Sn-Bi alloy under vacuum. This embedding prevents sample charging under the various microanalysis beams. Their surface was mechanically polished with SiC grids and with diamond suspensions down to 0.25 µm grade. A final step used a colloidal suspension of silica with a particle size of 0.02 µm. Fabrication characteristics, burn-up and main features are summarized in Table 2. These samples are all high burn-up fuels exhibiting HBS on their periphery and clear formation of fission gas bubbles, detectable by optical microscopy, in the central part of the pellets. Standard UO_2 fuels were examined, but also a Cr doped fuel where the dopant was added to promote the formation of large grains during the pellet sintering. The labels used here to name these specimens combine the type of fuels (Std or Cr) and the specimen rounded burn-up, expressed in GWd/t_U (61 to 73). Sample Std-73 is the same as that used in [34]. The porosities given in Table 2 are pellet fabrication data, deduced from immersion density measurement results, relatively to the theoretical densities without pores. They point out that the porosity was lower for the Cr doped fuel than for the Std fuels.

Figure 1 presents simplified linear power histories, at the axial elevation of the specimens studied, as a function of the irradiation time. It also gives the resulting temperature histories along the rod centerlines for this same level, as calculated by the fuel behavior code Alcyone [39,40]. The highest burn-up standard UO_2 sample (Std-73) underwent a linear power history where the second irradiation cycle was at low power (around 86 W/cm) whereas its sixth annual cycle had a long period around 190 W/cm, but a final around 120 W/cm. Specimen Std-61 had the highest linear powers, between 200 and 250 W/cm, during its three first annual cycles, and a last cycle mostly around 158 W/cm. Apart from Std-73, all high burn-up specimens were in the range 120 to 162 W/cm during their last cycle. It has to be noted that specimens Std-63 and Cr-63, irradiated together in the same subassembly, were both cut at levels where the local average section burn-up was lower than the rod average burn-up, whereas Std-61 and Std-73 were from the high burn-up parts of their rods. Std-73 and Std-61 were irradiated in reactors with refueling cycles of 12 months. It was 18 months for the other specimens.

The fission gas release fractions (FGR%), measured by rod puncturing, show a general increase with the rod burn-up, similarly to the results shown in [33].

When compared to the specimen used in [37] and [24], the fuel enrichments were higher (4.48 to 4.95% instead of 2.9%), the pellet diameters were smaller (8.086 to 8.192 mm instead of 9.06 mm) and the fission gas release fractions at high burn-up were higher.

Label	Burn-up (GWd/t_U)		Cladding	Fuel type (grain size µm)	^{235}U (%)	Pellet ∅ (mm)	As fabricated average porosity (%)	Final rod FGR (%)
	rod	specimen						
Std-61	56.7	61.4	Zr4	Standard (8.8)	4.48	8.193	4.0	2.8
Std-63	65.1	63.5	M5	Standard (9.1)	4.95	8.192	4.9	4.3
Std-73	67.5	72.7	M5	Standard (10.3)	4.49	8.086	4.7	6.2
Cr-63	63.7	62.7	M5	Cr doped (60.1 but smaller on periphery)	4.89	8.192	2.8	3.0

Table 2: Characteristics of the samples studied

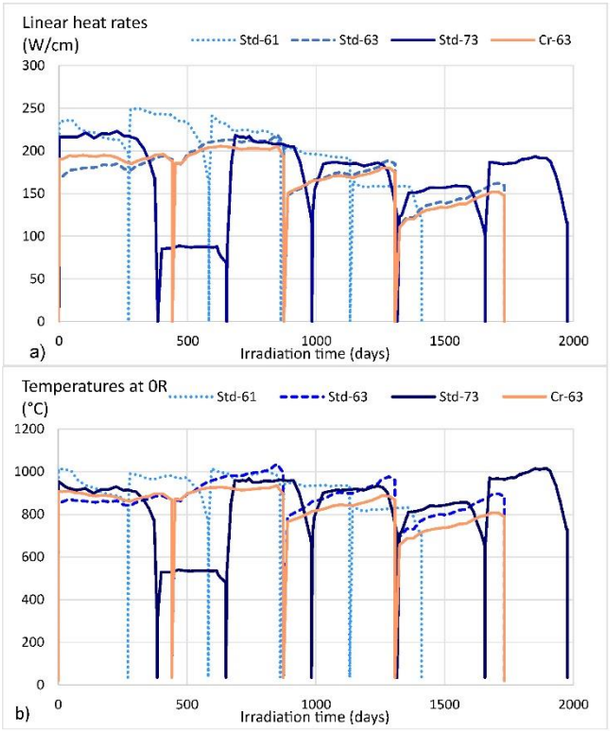

Figure 1: a) Simplified linear power and b) centerline temperature histories, at the specimen levels (Alcyone code calculations)

2.2 Examination devices

The FIB-SEM + EBSD used for this work is in the CEA Cadarache LECA-STAR hot-cell facility. It is inside a shielded cell and is connected to a glove box, also inside the cell, in order to prevent radioactive contamination [41,42]. It is a field emission electron gun Carl Zeiss Auriga 40. The devices used in this work were:

- A secondary electron secondary ion detector (SESI).
- An Orsay Physics COBRA focused ion beam (FIB) column,
- An Orsay Physics gas (Pt) injection system (GIS),
- An Oxford electron back scattered diffraction system (EBSD) with a Nordlys camera, for the parallel article [38].

The 3D FIB-SEM examination principle was similar to works exposed, for example, in [43,44].
In these 3D examinations, the thickness of the material sputtered by the FIB between each SEM image was the same as the pixel size of the SEM images. In the data processing, the grey level of a pixel on a SEM image was attributed to the whole corresponding voxel, i.e. a cube with the pixel size in two directions and the inter-image thickness in the other direction. As shown in Table 3, for most examinations, these voxels were 15 nm side cubes. This work is based on several hundreds of images. In addition to the results derived from these images, only a few of these images, of details from these images and 3D reconstruction views are included in the article. The main 3D views are associated with movies.

The main steps in the data processing were the image registration, the filtering of curtaining effect lines, "lighting" corrections and segmentation. Most of these data processing was conducted using the FIJI/ImageJ image processing and analysis platform [45-47], using of a series of our own plugins, tailored to our particular needs, mixed with existing plugins such as Image Stabilizer [48], Beat Xlib [49], MorpholibJ [50]

and BoneJ [51]. Image segmentation was conducted using Ilastik [52]. The 3D views shown here were built using 3D Slicer [53,54].

Most of this work is focused on the fission gas bubbles, on their sizes and shapes. For this work, the shape parameters and classes used are described in section 2.3. The bubble's volume is also one of the properties monitored in this work. Despite the fact that most bubbles in this work are far from spherical, it was found convenient to report these volumes by using the equivalent spherical diameter (*ESD*) i.e. the diameter of a sphere having the same volume as the considered bubble, whatever its shape.

2.3 Bubble shape classification

Considering the qualitative observations of the bubbles, shown in section 3, quantitative information was derived from these 3D examinations.

In this work, the volume distribution of the bubbles are given after volume classification into classes expressed through their *ESD*. Median sizes are given by the $ESD_{50\%}$, i.e. the diameter for which 50% of the volume of the considered bubbles is made of smaller bubbles and 50% of larger bubbles.

The volume reference used for the volume% or the bubble densities, is the volume of the examined box, after removal of the volume of the largest cavities very likely to be fabrication pore remnants. The examined volumes are clearly too small for a proper study of such fabrication pores. In these analyses, a cutoff at 0.038 µm (2.873×10^{-5} µm^3) was used. For the 3D examinations with 0.015 µm side voxels, this cutoff corresponds to excluding the objects made of less than 9 voxels.

Taking into account the qualitative observations of the bubbles, they were set into four shape classes:

- long bubbles,
- flat bubbles,
- compact bubbles and,
- complex bubbles.

These four classes were defined using three indicators linked to the bubble shapes and described hereafter:

- *Sphericity*,
- i_1/i_0 and
- i_2/i_1.

The *Sphericity* indicator was calculated using the formula:

$$Sphericity = 36\pi\frac{V^2}{A^3} \quad (1)$$

where V is the bubble volume and A the bubble surface area. This indicator, with no dimension, is a value within the interval]0, 1].The value 1 is that of a perfect sphere. Low values correspond to bubbles far from spherical. This indicator, commonly used, has a 2D equivalent which is the circularity indicator. This circularity indicator (also called "isoperimetric deficit index" or "shape factor") is: $circularity = \frac{4\pi a}{p^2}$, where a is the area of the object in the examined plane and p is its perimeter. In the case of the fuel bubbles, this *Sphericity* indicator cannot be used alone to evaluate how close to a sphere a bubble can be. This has to do with the smoothness or roughness of the bubble surfaces that can lead to very different surface areas for objects that can have very similar general shapes. This is easily understood using a 2D illustration: in Figure 2, shape b can be considered as close to a disc, but its circularity indicator is low and similar to that of shape c, very far from a disc, shape a.

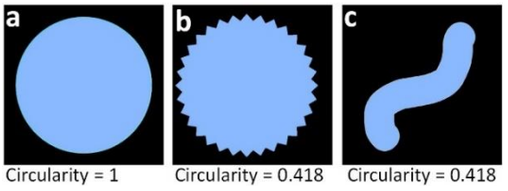

Figure 2: 2D Example showing the values taken by the circularity indicator for three shapes a, b and c, to illustrate the effect of the bubble surface state on the 3D Sphericity indicator

In this work, the volume V of a bubble is the sum of the volume of all the voxels constituting this bubble, and its area A is computed using the Crofton formula [55,56].

The two indicators i_1/i_0 and i_2/i_1 refer to the three lengths of a minimal rectangular cuboid bounding box enclosing a bubble. i_0 is the length of the longest side of the box, i_1 that of the intermediate side and i_2 that of the shortest side, as illustrated in Figure 3.

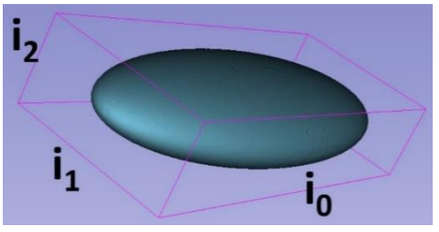

Figure 3: Illustration of the meaning of the values i_0, i_1 and i_2 used in bubble shape classification. The bounding box used is not the x, y, z bounding box of the 3D FIB images, but the minimal volume oriented box with orientations adapting to each bubble.

Combining these three indicators:

- Long bubbles are those showing $\frac{i_1}{i_0} \in]0, 0.4]$ whatever their *sphericity* or $\frac{i_2}{i_1}$ values,
- Flat bubbles are those showing $\frac{i_1}{i_0} \in]0.4, 1]$ and $\frac{i_2}{i_1} \in]0, 0.4]$ whatever their *sphericity,*
- Compact bubbles are those showing $\frac{i_1}{i_0} \in]0.4, 1]$ $\frac{i_2}{i_1} \in]0.4, 1]$ and $sphericity \in]0.2, 1]$,
- Complex bubbles are those showing $\frac{i_1}{i_0} \in]0.4, 1]$ $\frac{i_2}{i_1} \in]0.4, 1]$ and $sphericity \in]0, 0.2]$.

This principle is illustrated in Figure 4, with color boxes showing the conditions for a bubble to be classified into one or the other of the four classes according to the values taken by the three indicators. This figure also gives, for each class, one example taken among the studied sample bubbles. For these examples it gives the values taken by the three indicators, the sample it comes from, and the *ESD* of the bubble used. In the studied samples, many bubbles lay close to one or the other of these borders. They can therefore be close in shape to other bubbles on the other side of the border. Therefore, these bubble types must not be considered as very separated populations, nevertheless, they allow to follow major differences between samples and radial positions.

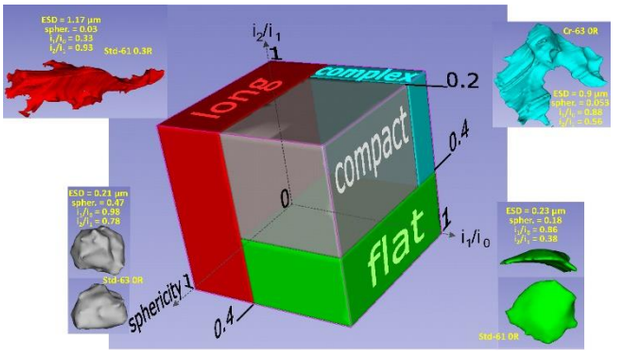

Figure 4: Classification principle of the bubbles according to their sphericity, elongation and flatness

Nota bene: This 3D FIB-SEM work must be considered as giving ranges of magnitude in the numbers given and general trends in the mechanisms involved in the fission gas behavior at high burn-up rather than providing very reliable and precise numbers that can be trustfully used in fuel behavior code validation:

- The volumes examined are too small to properly cover the whole bubble size range present in these samples. This is particularly true for the Std-73 sample and for grain edge bubbles. In the largest size classes for which results are given here, the number of bubbles really found is low and the statistical reliability is poor.
- Despite the cutoff, the bubble density values for the *ESD* 0.038 to 0.1 µm class might be impacted by defects both ways in the detection of the smallest bubbles.
- The phenomenon, known as pore back effect, leading to bright grey levels sometimes showing inside large bubbles when their bottom comes close to the cut surface (see **Error! Reference source not found.**) was taken into account in the bubble segmentation process, but does lead to uncertainties on the exact volumes and shapes of some of the bubbles.
- The FIB 3D process itself it not isotropic. If a piece of matter is cut from the rest of the sample, it falls away before having been fully milled slice by slice. Figure 5 illustrates on the same "bubble" how the FIB cutting progressing from right to left or from left to right modify differently the shape and volume of the bubble. It leads to flatter surfaces for the fronts of the bubbles than for their backs.

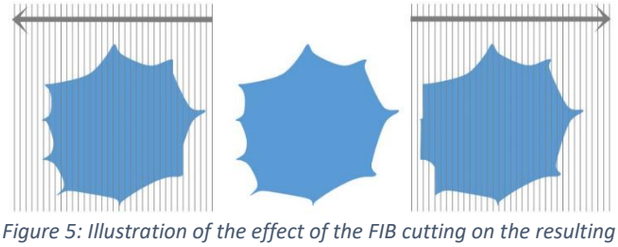

Figure 5: Illustration of the effect of the FIB cutting on the resulting bubble shape

3. FIB-SEM images forming the 3D examinations

3.1 Global views

Table 3 gives, for each specimen, the radial positions, volume sizes and voxel sizes, of the FIB-3D studied volumes. These volumes are classified as being:

- in the center of the pellets, for fields where a high fission gas bubble formation occurred,
- in the intermediate zone between the central area and the HBS transition zone + HBS rim.

Name	3D FIB radial position (r/R)		Volume (µm³)	Voxel size (nm³)
Std-61	center	0	11.1×10.4×6.4	15×15×15
		0.30	11.9×8.9×9.4	15×15×15
	intermediate	0.57	11.9×10.2×6.7	15×15×15
Std-63	center	0	20.3×8.3×3.2	10×10×10
Std-73	center	0	28×10.6×5	17×17×17
		0.35	25.5×14×4.9	15×15×15
Cr-63	center	0	10×4.8×7.1 19×9.9×3.3	15×15×15 20×20×20
		0.30	11×6.5×9	15×15×15
	intermediate	0.50	11×5.8×9	15×15×15

Table 3: 3D FIB-SEM examination radial positions, volume sizes and voxel sizes

Figure 6 gives one typical example of a 2D SESI image forming the image stacks for each 3D FIB-SEM examination listed in Table 3.

In these SEM images:

- the darkest pixels correspond to holes on the surfaces, i.e. intragranular or intergranular fission gas bubbles, or pores remaining from the pellet's sintering,
- the brightest pixels mainly correspond to metallic fission product precipitates, typically made of Mo, Tc, Ru, Rh and Pd. Nevertheless, some hole edges or bottoms can also lead to bright pixels (pore back effect), making the segmentation of the 3D images more complicated,
- the grey levels in between correspond to the irradiated UO_2 itself, with influences of the surface state and of the local crystal orientation, through differences in the electron channeling. Typically, in classical 2D polished sample examinations, like that used in [32], the grain grey level contrasts were only obtained after the final step using a colloidal suspension of silica. Without this final step, the defects induced by the rougher polishing would homogenize the grain-to-grain grey levels.

In all these fuels, in the center, the EBSD examinations [38] showed the restructuring into sub-grains at various degrees, and, in the intermediate zone, the absence of such restructuring. Consistently, in these images, within the original grains, in the field where intragranular bubbles are visible, the grey levels changes form small patches. This is due to electron channeling differences induced by the local crystal orientation differences. It appears more clearly for the Std-61 at 0.3R, Std-73 at 0R and 0.35R and for Cr-63 at 0R and 0.3R than for Std-61 at 0R and Std-63 at 0R. This reflects differences in the restructuring degree, measured by EBSD, but also certainly tiny differences in the use of the FIB and SEM, these examinations having been conducted over the three first years of operation of the FIB-SEM, after its hot cell commissioning. In these 2D images, many bubbles inside the original grains exhibit shapes that are not compatible with spherical bubbles. This is less obvious for Std-63 at 0R. In the Cr-63 0R image, an absence of restructuring and a lower porosity are visible in layers of about 1 µm around the grain boundaries. This is also consistent with the EBSD results on this sample. The image also shows the presence of metallic fission product precipitates, the largest ones being generally along the initial grain boundaries.

In the two fields outside the central zone, i.e. in the intermediate zone, for Std-61 at 0.57R or Cr-63 at 0.5R, the SEM images are also consistent with this absence of restructuring measured in [38]. In these fields small metallic fission product precipitates (<0.08 µm) are detected along or around the grain boundaries. On the right of the image Cr-63 at 0.5R, the high density of small metallic fission product precipitates corresponds to the presence of a grain boundary in a plane forming a low angle with that of the image.

In the following sections, detailed images extracted from these image stacks, are shown together with 3D views of the bubbles as extracted from small volumes. Section 3.2 shows the bubbles from volumes inside the original grains, thus showing intragranular bubbles. Section 3.3 shows bubbles on original grain boundaries, i.e. intergranular bubbles.

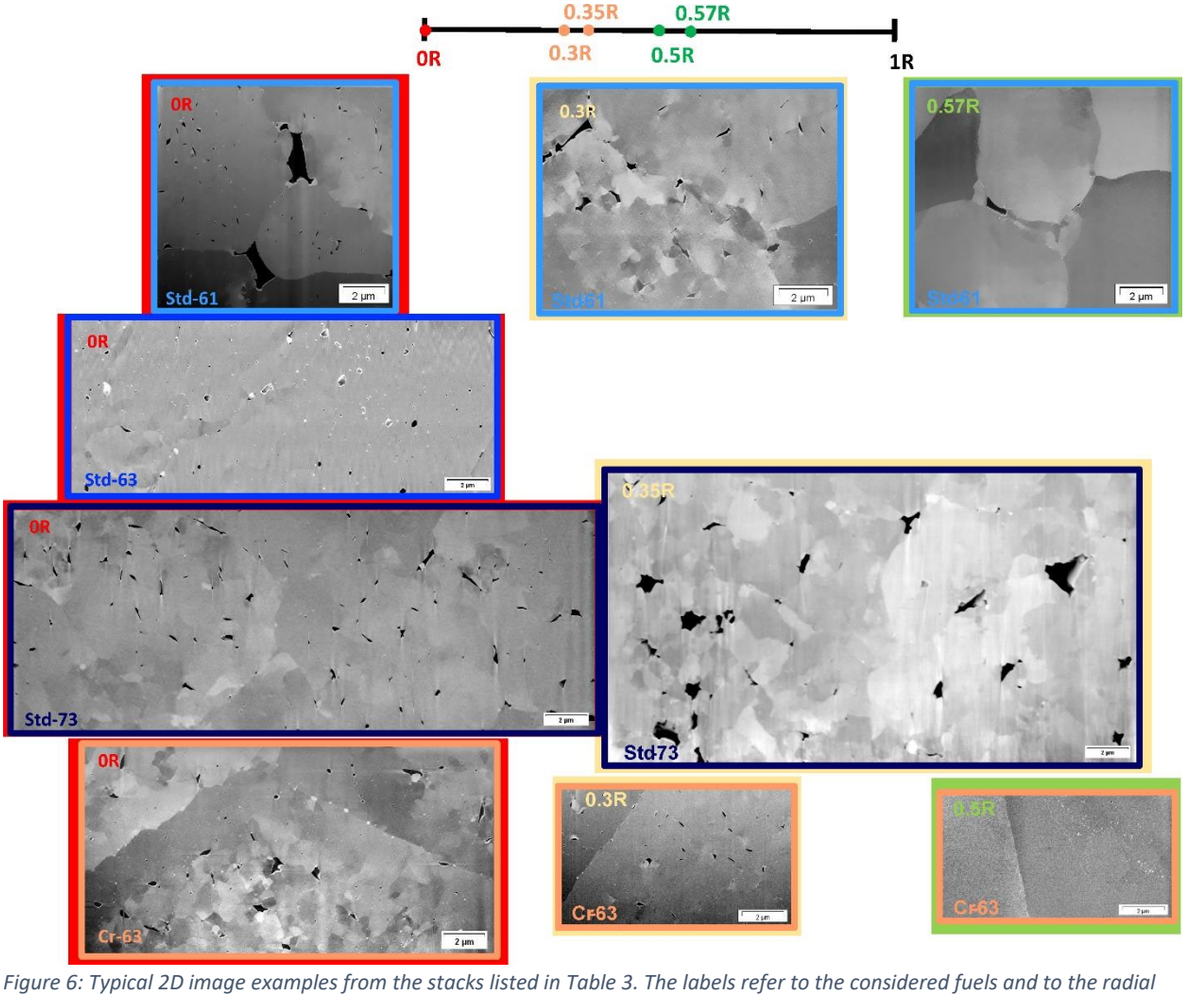

Figure 6: Typical 2D image examples from the stacks listed in Table 3. The labels refer to the considered fuels and to the radial location of the FIB-SEM 3D examination

3.2 Intragranular bubbles

Figure 7 a) shows a detailed image covering 2.6×2.4 µm^2 cut inside an original grain in the stack taken at **0R in the Std-61 sample**. It shows the presence of flat lenticular bubbles. Figure 7 b) gives two perpendicular views of the 3D extraction of these bubbles over a volume of 2.6×2.4×1.5 µm^3 including the example of Figure 7 a) and cut inside one of the original grains, avoiding the original grain boundaries. This same 3D detailed volume was used to produce the movie associated to Figure 7 b) (Multimedia view).

In this volume, the most visible bubbles are flat, lenticular type. The bubbles have a diameter around 0.3 µm and a thickness around 0.07 µm. The $ESD_{50\%}$ of these flat intergranular bubbles, measured over the whole studied volume, is 0.17 µm. In addition to these bubbles, there are smaller and more compact bubbles, and also bubbles in the same size range, but more compact. Over the whole studied volume, the $ESD_{50\%}$ of these compact bubbles is of 0.19 µm. The flat lenticular bubbles are very far in shape from the spherical bubbles one would expect inside the grains. They actually look like small intergranular bubbles and are likely to be on boundaries between sub-grains despite the absence of such evidence in the grey levels surrounding them. They are also very different from the more complex bubbles shown in [34] for the Std-73 sample, even though part of the largest intragranular bubbles found were classified as complex, with an $ESD_{50\%}$ of 0.25 µm. The flat and complex bubbles form 21% and 11.4% of the intragranular bubble volumes while the more compact bubbles constitute 64.2% of them. These bubbles in the compact class, often appear as flat bubbles, slightly too thick to be in the flat class. Most bubbles appear to be associated to metallic fission product precipitates. For the lenticular bubbles, these precipitates tend to be on the disc rim, thus suggesting a preferential arrival along the planes on which these bubbles are.

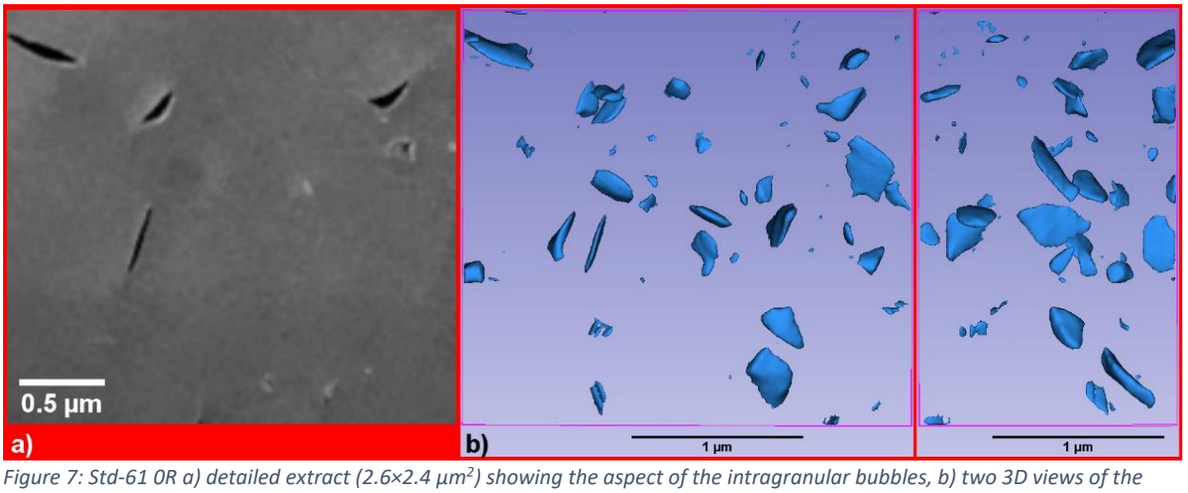

Figure 7: Std-61 0R a) detailed extract (2.6×2.4 µm^2) showing the aspect of the intragranular bubbles, b) two 3D views of the intragranular bubbles in a corresponding detailed extract (2.6×2.4×1.5 µm^3) (Multimedia view)

For intragranular bubbles in the **Std-63 sample at 0R**, an equivalent detailed image, is given in Figure 8 a). The intragranular extract also covers 2.6×2.4×1.5 µm^3, with 3D views in Figure 8 b) (Multimedia view). In this sample, the situation is quite different, with less flat bubbles and more compact bubbles, yet far from spherical. These images show the presence of rare large bubbles with an *ESD* around 0.25 µm, but also a high density of smaller bubbles also rather compact, with an *ESD* below 0.1 µm. Over the whole studied volume, the intragranular compact bubbles constitute 71% of the intragranular bubble volumes with an $ESD_{50\%}$ of 0.19 µm, that of the bubbles set as complex, 25% with an $ESD_{50\%}$ of 0.35 µm, while flat bubbles form 2.4%.

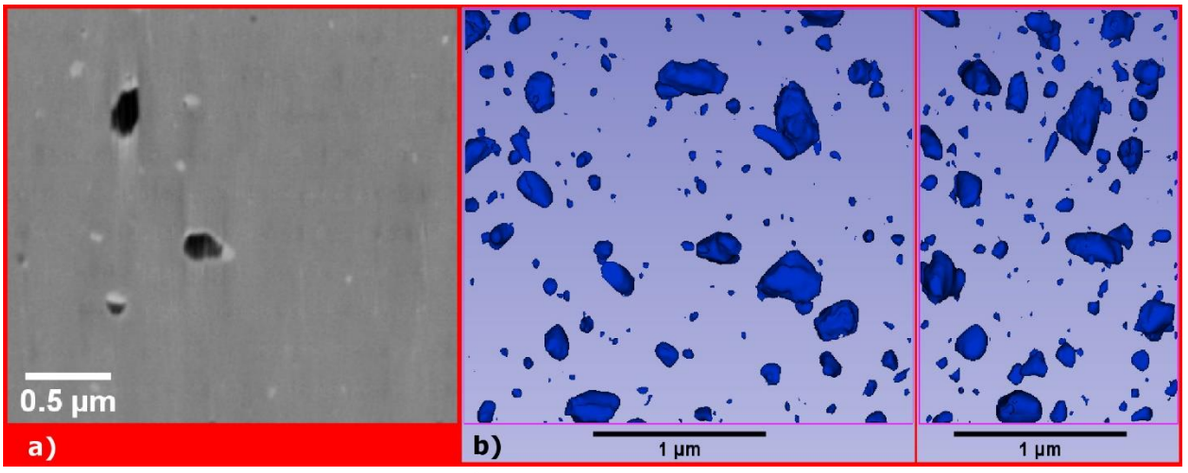

Figure 8: Std-63 0R, a) detailed extract (2.6×2.4 µm²) showing the aspect of the intragranular bubbles, b) two 3D views of the intragranular bubbles in a corresponding detailed extract (2.6×2.4×1.5 µm³). (Multimedia view).

For the highest burn-up studied here, in the **Std-73 sample at 0R**, the example given in Figure 9 a) and b) (Multimedia view) covers a larger volume 5.2×4.6×3 µm³. This larger volume was necessary because of the presence of larger intragranular bubbles in this fuel. As shown in [34], very complex intragranular bubbles were found. These complex bubbles are widely made of relatively flat parts. In fact, more simple flat bubbles are also present, yet often larger and less regular in shape than those found in the Std-61 at 0R, with an *ESD* around 0.3 µm, and diameters that can be higher than 1 µm. Compact bubbles, with a wide variety of sizes, are also present. Over the whole studied volume, the complex bubbles constitute 61% of the intragranular bubbles volumes, with an $ESD_{50\%}$ of 0.38 µm, the flat bubbles 19% and an $ESD_{50\%}$ of 0.30 µm, while compact bubbles with an $ESD_{50\%}$ of 0.19 µm form 17% of this volume.

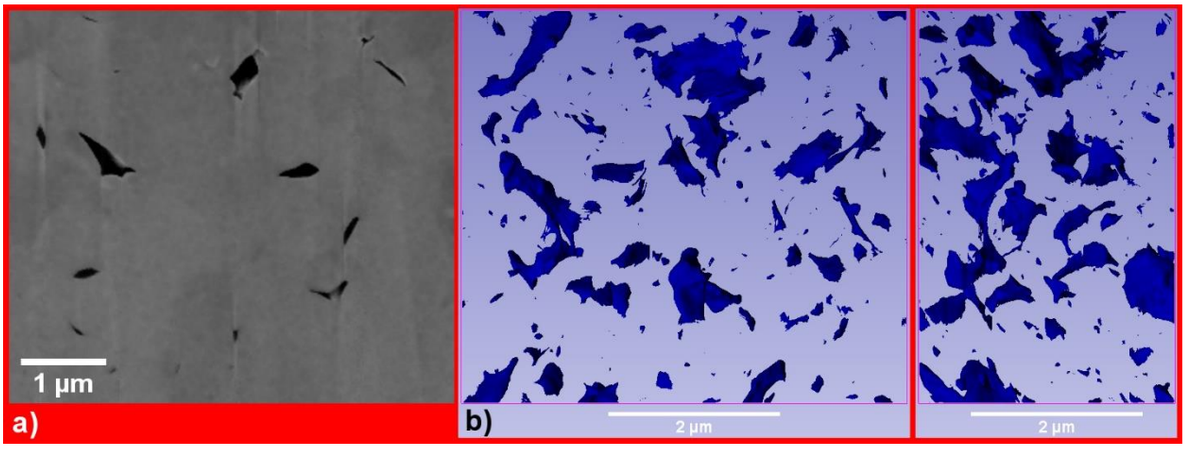

Figure 9: Std-73 0R, a) detailed extract (5.2×4.6 µm²) showing the aspect of the intragranular bubbles, b) two 3D views of the intragranular bubbles in a corresponding detailed extract (5.2×4.6×3 µm³). (Multimedia view)

For the **Cr-63 sample at 0R**, the same larger volume of 5.2×4.6×3 µm³ was chosen for an intragranular example, due to the large sizes of some of the bubbles (Figure 10 a) and b) (Multimedia view). On these images, the large intragranular bubbles are all clearly set on the boundaries between the new sub-grains. Their shapes are also clearly influenced by the sub-grains surrounding them, and all the sub-grain boundaries emerging on their surface. Various shapes are present. Some are quite complex. Some are relatively flat. Others are more compact, despite their shapes far from spherical, and influenced by the sub-grains and boundaries surrounding them. In addition to these large bubbles, with an *ESD* that can

reach 0.9 µm, much smaller and compact bubbles are also present, with an *ESD* below 0.1 µm. Many of these small bubbles appear to also be on boundaries, but some of these smallest bubbles seem to be intra-sub-grains. Over the two volumes studied at 0R, the intragranular complex bubbles form 49.4% of the intragranular bubble volumes, with an $ESD_{50\%}$ of 0.67 µm, the flat bubbles 11.2%, with an $ESD_{50\%}$ of 0.57 µm and compact bubbles 39% with an $ESD_{50\%}$ of 0.46 µm.

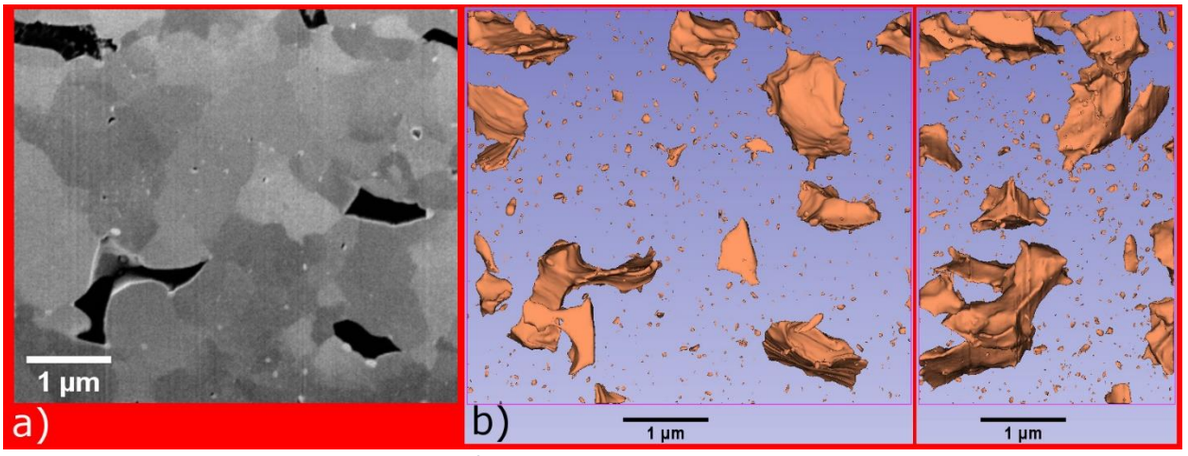

Figure 10: Cr-63 0R, a) detailed extract (5.2×4.6 µm^2) showing the aspect of the intragranular bubbles, b) two 3D views of the intragranular bubbles in a corresponding detailed extract (5.2×4.6×3 µm^3). (Multimedia view)

At **0.3R**, the **Std-61 intragranular** example volume of 3.49×3.17×2 µm^3, Figure 11 a) and b) (Multimedia view), also clearly shows the presence of large, inter-sub-grain bubbles. These bubbles can be flat, but with diameters larger than in the same sample at 0R, around 0.7 µm, and also with thicker parts reaching ~0.18 µm and *ESD* values around 0.3 µm. More complex bubbles, widely made of such flat parts, reach larger *ESD* values, 0.52 µm for the largest bubble in this example. Smaller bubbles also exist, often on boundaries. Over the whole studied volume, complex bubbles form 50% of the intergranular bubble volume, with an $ESD_{50\%}$ of 0.38 µm, flat bubbles 31.2%, $ESD_{50\%}$ of 0.28 µm and compact bubbles 15.9%, $ESD_{50\%}$ of 0.21 µm.

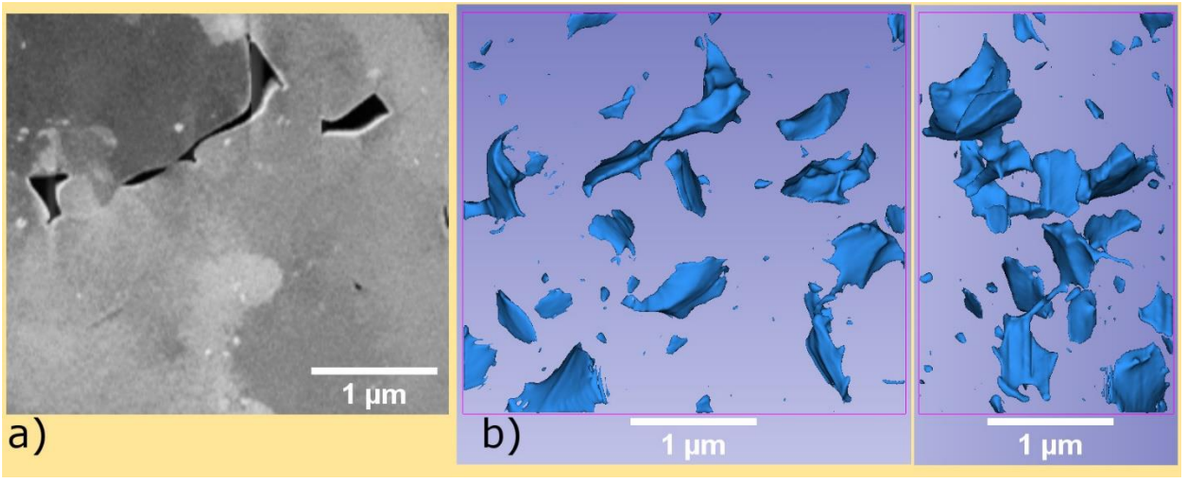

Figure 11: Std-61 0.3R, a) detailed extract (3.49×3.17 µm^2) showing the aspect of the intragranular bubbles, b) two 3D views of the intragranular bubbles in a corresponding detailed extract (3.49×3.17×2 µm^3). (Multimedia view)

At **0.35R, in the Std-73 sample**, a 5.2×4.6×3 µm^3 volume presented in Figure 12 a) and b), (Multimedia view), mainly shows large complex intragranular, but inter-sub-grain, bubbles, with *ESD* values that can be higher than 1 µm. Smaller bubbles are also present, but there are not many of them and they also appear to be inter-sub-grains. Compared to the same sample at 0R, there is a lower density of bubbles, but with larger bubbles. Over the whole studied volume, the complex bubbles form 81.7% of the intragranular bubbles, with an $ESD_{50\%}$ of 0.86 µm, the flat bubbles 6.4%, $ESD_{50\%}$ of 0.50 µm and compact bubbles 11.5%, $ESD_{50\%}$ of 0.44 µm.

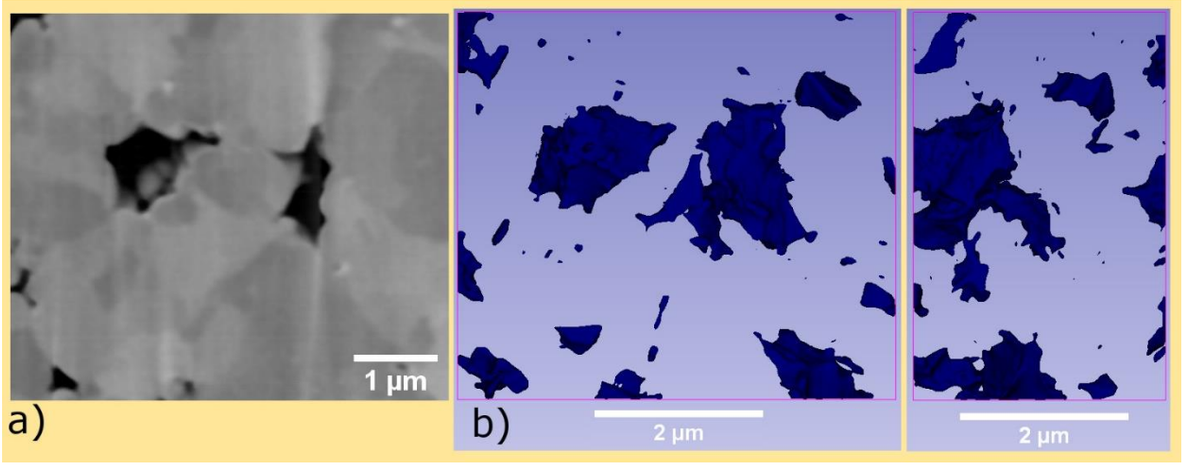

Figure 12: Std-73 0.35R, a) detailed extract (5.2×4.6 µm^2) showing the aspect of the intragranular bubbles, b) two 3D views of the intragranular bubbles in a corresponding detailed extract (5.2×4.6×3 µm^3). (Multimedia view)

At **0.3R, the Cr-63 sample,** the intragranular 5.2×4.6×3 µm^3 detail Figure 13 a) and b) (Multimedia view), exhibits a high density of small flat bubbles with *ESD* values around 0.25 µm, diameters of less than 0.5 µm and thicknesses below 0.1 µm. There are no large and complex bubbles as observed at 0R in the same sample. The situation is therefore quite different from that of the Std-61 and Std-73, for which larger bubbles where found at 0.3R or 0.35R than at 0R. Over the whole studied volume, the flat bubbles make 46.6% of the intragranular bubble volume, with an $ESD_{50\%}$ of 0.20 µm, the compact bubbles 34.6%, $ESD_{50\%}$ of 0.19 µm and the complex bubbles 16.9% with an $ESD_{50\%}$ of 0.25 µm.

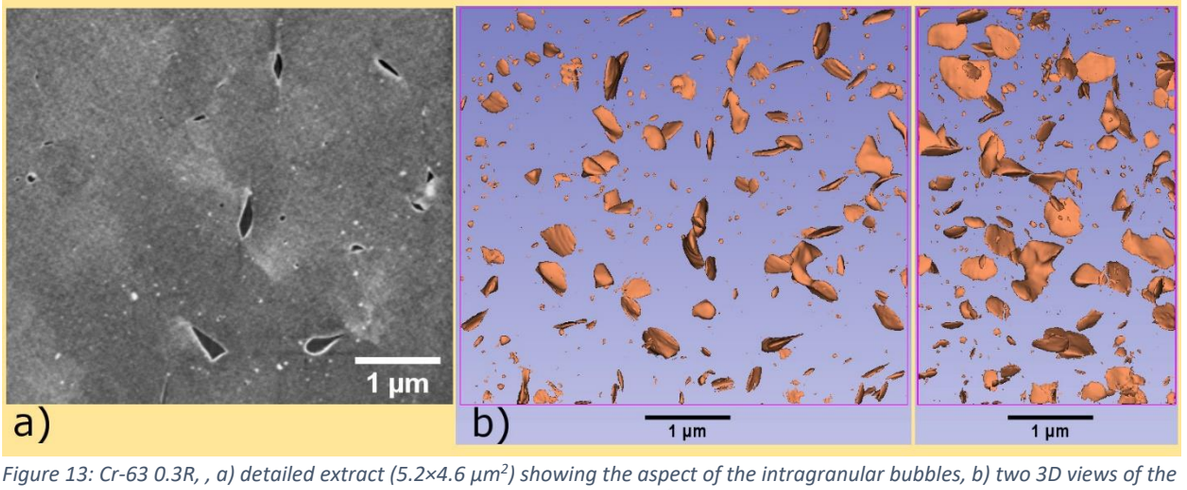

Figure 13: Cr-63 0.3R, , a) detailed extract (5.2×4.6 µm^2) showing the aspect of the intragranular bubbles, b) two 3D views of the intragranular bubbles in a corresponding detailed extract (5.2×4.6×3 µm^3). (Multimedia view)

3.3 Intergranular bubbles

In this section, the details extracted from the large image stacks and the detailed 3D views are meant to illustrate the situation of the bubbles that are clearly on original grain boundaries or on original grain edges (the intersection line of three grain boundaries). Cavities that were likely to be bubbles formed during the irradiation rather than fabrication pore remains were selected.

Figure 14 and Figure 15, both for **Std-61 at 0R**, give examples respectively on grain faces and along grain edges. The regular intergranular bubbles, of various sizes, are isolated closed bubbles. On the largest bubble, it is also interesting to see the effect on its shape of the boundaries between sub-grains, emerging on the surface and forming ridges. On the grain edges, Figure 15, long bubbles were found, but, being closed, they appear not to form long interconnected networks.

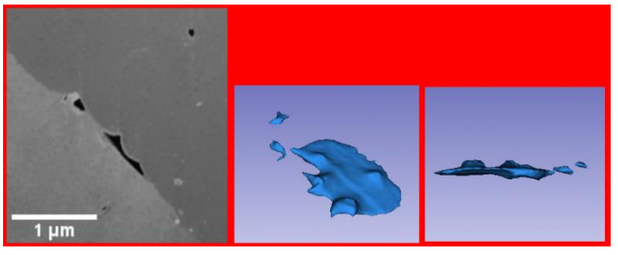

Figure 14: Std-61 at 0R, detailed images on intergranular bubbles and associated 3D views showing that these bubbles on grain faces, are closed

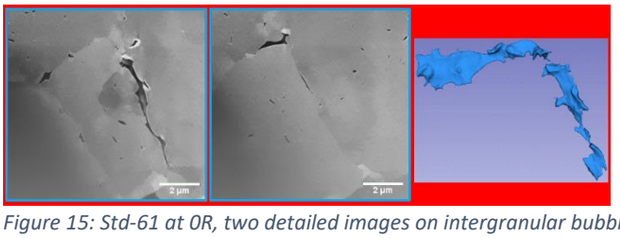

Figure 15: Std-61 at 0R, two detailed images on intergranular bubbles and associated 3D views showing that these two long bubbles, on grain edges, are closed

The example for **Std-63 at 0R** shows, in Figure 16, a regular intergranular bubble on the left side of the detailed image and a grain edge bubble on its right. Both bubble types are isolated and closed.

Figure 16: Std-63 at 0R, detailed image on intergranular bubbles and associated 3D views showing that these bubbles, small or large, are closed, even that on grain edges (on the right on the micrograph and on the first 3D view

Similarly, Figure 17, for the **Std-73 sample at 0R**, the regular grain face intergranular bubbles and the grain edge bubble in this example are closed bubbles. On the largest two of them, again, the effect of the surrounding sub-grain boundaries is visible, forming ridges on the surface.

Figure 17: Std-73 at 0R, detailed image on intergranular bubbles and associated 3D views showing that these bubbles, small or large, are closed, even that on grain edges (on the right on the micrograph and on the 3D views)

In the **Cr-63 sample at 0R**, only few intergranular bubbles were detected on the two grain boundary surfaces in the 19×9.9×3.3 µm^3 volume examined. Figure 18 shows one of the complete 2D image, similar to that shown in Figure 6. It exhibits a few small intergranular bubbles, and also metallic fission product precipitates. The two views of the 3D reconstruction in Figure 18 give the same point of view, one with the bubbles only, the other with the bubbles and the metallic fission product precipitates, represented in green. This point of view was set along the direction of the grain edge line, i.e. on the intersection between the two grain boundaries. This point of view clearly evidences the low density of bubbles in a layer around the grain boundaries, already mentioned in section 3.1. They also confirm that only a few bubbles were on the grain boundaries themselves. Moreover, the view with the metallic fission product precipitates shows that, as for bubbles there was a clearly lower density of metallic fission product precipitates within the same layers in which a low bubble density was found, around the grain boundaries. However, unlike bubbles, there was a high density of these precipitates on the grain boundaries themselves. In this volume, only a short length of 0.87 µm of grain edges was present. On this short length we find the end of a grain edge bubble: there is no grain edge bubble on 0.24 µm of the length of the grain edge while the rest of it is covered by a bubble 0.63 µm long in the examined volume (seen perpendicularly on the views of the 3D reconstruction, at the intersection between the two grain boundary planes).

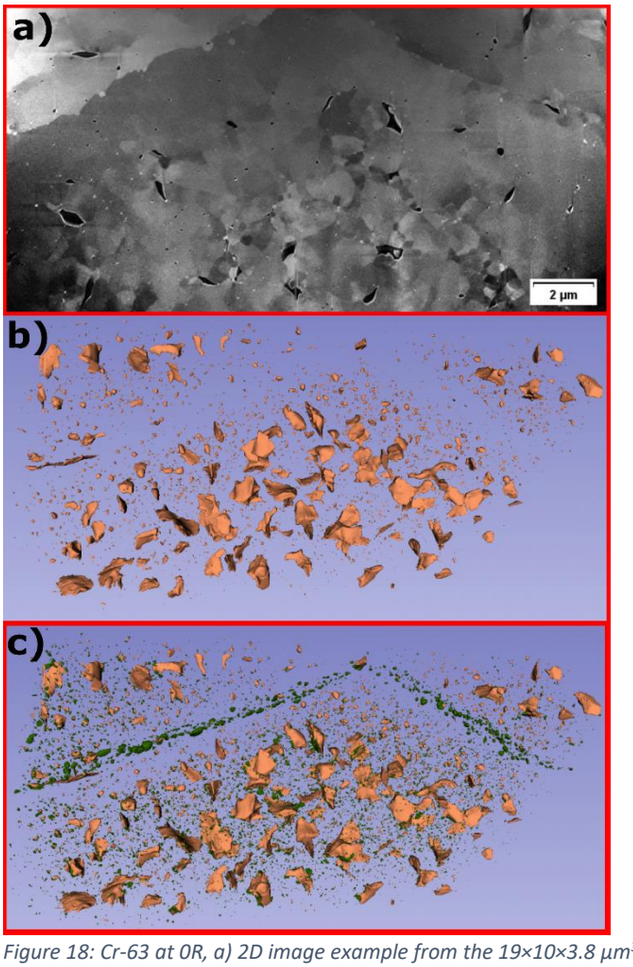

Figure 18: Cr-63 at 0R, a) 2D image example from the 19×10×3.8 µm³ stack and 3D views b) of the bubbles c) of the bubbles and the metallic precipitates seen from a grain edge line

At **0.3R, on the Std-61 sample**, the large intergranular bubbles, Figure 19, show again the effect of the surrounding sub-grains, of the boundaries between them and of metallic precipitates, on the shape of the bubble surfaces. These bubbles can spread on several microns or be on the grain edges, but do not form an interconnected network.

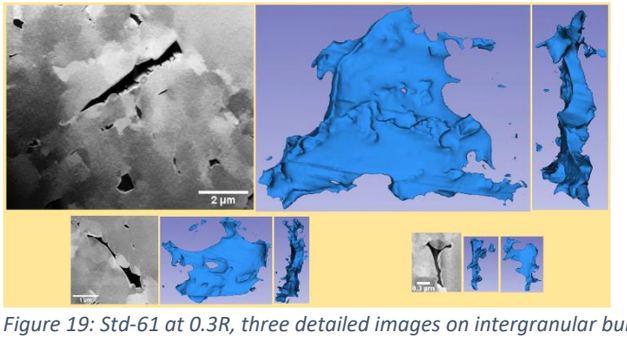

Figure 19: Std-61 at 0.3R, three detailed images on intergranular bubbles and associated 3D views showing that these bubbles, different in sizes, are complex but closed

At **0.35R on the Std-73 sample**, some of the intergranular bubbles took very complex shapes (Figure 20), similar to those of the intragranular bubbles, influenced by the surrounding sub-grains and boundaries

between the sub-grain. They are closed, even along the grain edges, but appear like the local interconnections, by thin tunnels, of thick complex bubbles.

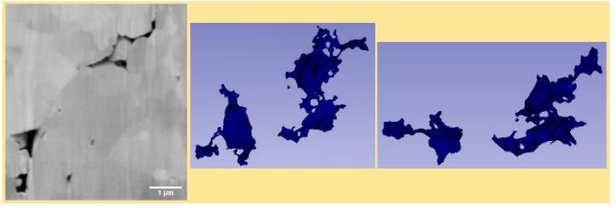

Figure 20: Std-73 at 0.35R, detailed image on intergranular bubbles and associated 3D views showing that these bubbles are complex but closed, even on grain edges

In the 11×6.5×9 μm^3 volume of the **Cr-63 sample at 0.3R**, three grain boundaries were present and a grain edge was examined over a length of 7.46 µm, Figure 21. As for Figure 18 at 0R, the first two 3D views have a point of view along the grain edge line, on the intersection between the three grain boundaries. They also come by pairs, without and with the metallic fission product precipitates represented in green. These views confirm the lowest bubble density in layers around the boundaries. This effect, however, seems to be lower on one side of one of the boundaries (left of the lowest boundaries in Figure 21 c). Again, a similar effect exists for metallic fission product precipitates, with an accumulation on the grain boundaries. Figure 21 e) and f) show a view of one of the three grain boundaries. On these boundaries, intergranular bubbles are present, often with complex shapes. They can spread over more than one micron, but do not form an interconnected network. Figure 21 b) e) and f) also show two long bubbles along the grain edge. They are interrupted inside this volume. Figure 21 a) plane was set in the section where there is no bubble along the grain edges. As at 0R, the examined volume is large enough to show the absence of a continuous grain edge network, but is far too small to give a complete view of the situation, considering the presence of long bubbles there.

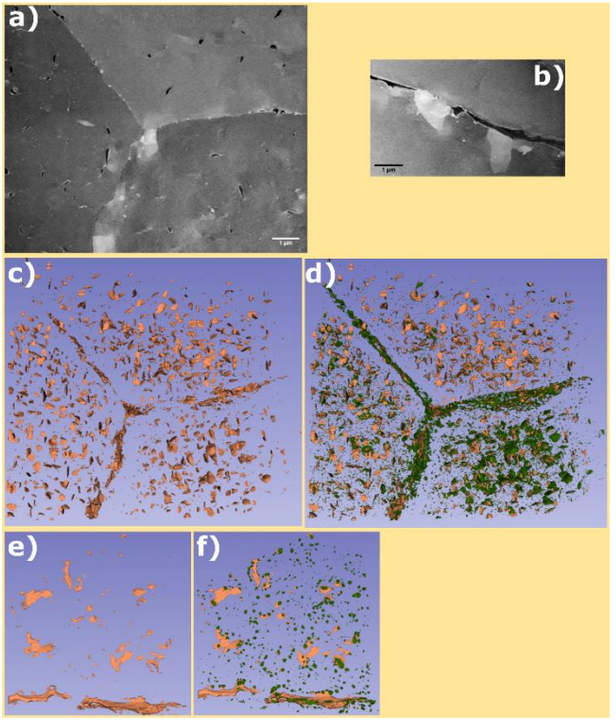

Figure 21: Cr-63 at 0.3R, a) 2D image top view resliced from the 11×6.5×9 µm³ stack, b) view along the grain edge, and 3D views c) of the bubbles d) of the bubbles and the metallic precipitates seen from a grain edge line, e) and f) views of the bubbles without and with the metallic precipitates, of the flattest of the three grain boundaries, including the grain edge

4. FIB-SEM 3D fission gas bubble shape classification

Using the shape classification described in section 2.3 and the same color rule as in Figure 4, (compact bubbles in grey, flat bubbles in green, long bubbles in red and complex bubbles in light blue), Figure 22 shows 3D views of the volume examined, for the four samples and for the radial positions in the central area (see Table 3). Each one of these views Figure 22 a) (Multimedia view), b) (Multimedia view), c) (Multimedia view), d) (Multimedia view), e) (Multimedia view), f) (Multimedia view), g) (Multimedia view), h) (Multimedia view) is associated with a movie. Most of the differences pointed out with the detailed images in section 3.2 are visible in these views. They are better quantified in the graphs Figure 24 and Figure 25.

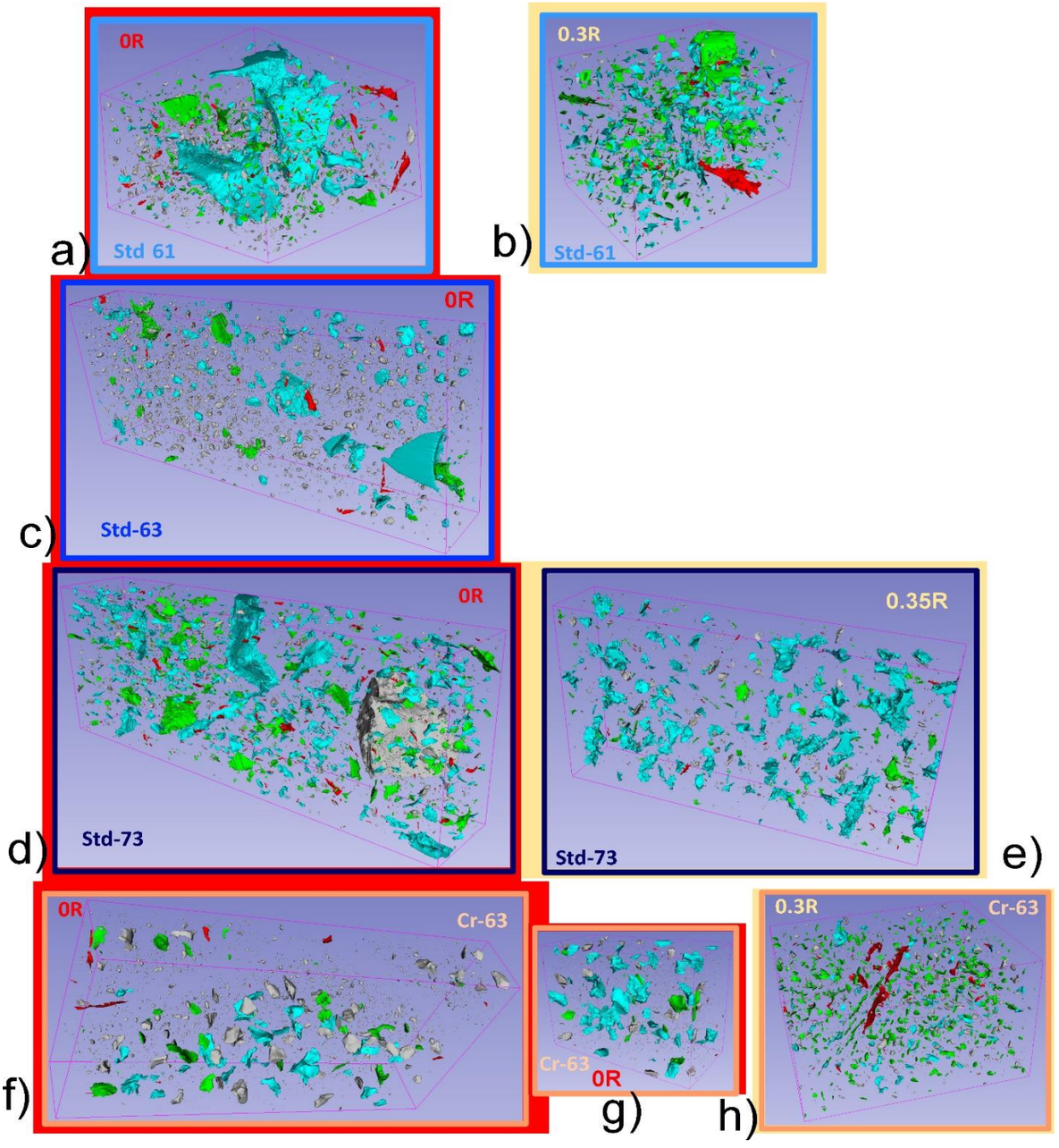

Figure 22: 3D views of the bubbles detected in the examined volumes for the four samples and for the central area field. The colors attributed to each bubble correspond to its shape classification with the same rule as in Figure 4: compact bubbles in grey, flat bubbles in green, long bubbles in red and complex bubbles in light blue. Figure 22 a) (Multimedia view), b) (Multimedia view), c) (Multimedia view), d) (Multimedia view), e) (Multimedia view), f) (Multimedia view), g) (Multimedia view), h) (Multimedia view) are each associated with a movie.

Table 4 gathers global results obtained on intragranular bubbles on these volumes, for the four shape classes studied. These results, show quantitatively the significant differences between the samples and between the studied volumes in the same sample. Figure 23 plots the $ESD_{50\%}$ of the intragranular bubbles for these studied volumes. For the Std samples, it shows the higher bubble sizes at 0.3R or 0.35R, relatively to 0R. It shows the opposite for the Cr sample.

	All intragranular bubbles	Compact	Flat	Long	Complex
Std-61 0R					
% volume	0.43%	0.28%	0.09%	0.02%	0.05%
Fraction of intragranular bubbles %		63.7%	21.3%	3.5%	11.5%
$ESD_{50\%}$ (µm)	0.19	0.19	0.17	0.20	0.25
Bubble/m^3	4.31×10^{18}	3.20×10^{18}	7.72×10^{17}	2.30×10^{17}	1.06×10^{17}
Std-61 0.3R					
% volume	0.70%	0.11%	0.22%	0.02%	0.35%
Fraction of intragranular bubbles %		15.9%	31.2%	2.9%	50.0%
$ESD_{50\%}$ (µm)	0.33	0.21	0.28	0.59	0.38
Bubble/m^3	2.70×10^{18}	1.60×10^{18}	6.72×10^{17}	1.98×10^{17}	2.22×10^{17}
Std-63 0R					
% volume	0.77%	0.54%	0.02%	0.01%	0.19%
Fraction of intragranular bubbles %		70.7%	2.4%	1.8%	25.1%
$ESD_{50\%}$ (µm)	0.24	0.19	0.38	0.28	0.35
Bubble/m^3	1.18×10^{19}	1.14×10^{19}	1.67×10^{17}	9.17×10^{16}	2.24×10^{17}
Std-73 0R					
% volume	0.59%	0.10%	0.11%	0.02%	0.36%
Fraction of intragranular bubbles %		16.7%	18.7%	3.7%	61.0%
$ESD_{50\%}$ (µm)	0.34	0.21	0.30	0.23	0.38
Bubble/m^3	1.94×10^{18}	1.04×10^{18}	4.43×10^{17}	2.09×10^{17}	2.52×10^{17}
Std-73 0.35R					
% volume	1.41%	0.16%	0.09%	0.01%	1.15%
Fraction of intragranular bubbles %		11.5%	6.4%	0.5%	81.7%
$ESD_{50\%}$ (µm)	0.83	0.44	0.50	0.20	0.86
Bubble/m^3	9.58×10^{17}	6.57×10^{17}	1.55×10^{17}	7.40×10^{16}	7.23×10^{16}
Cr-63 0R					
% volume	1.64%	0.64%	0.18%	0.01%	0.81%
Fraction of intragranular bubbles %		39.0%	11.2%	0.5%	49.4%
$ESD_{50\%}$ (µm)	0.58	0.46	0.57	0.16	0.67
Bubble/m^3	8.00×10^{18}	7.34×10^{18}	3.64×10^{17}	2.01×10^{17}	9.32×10^{16}
Cr-63 0.3R					
% volume	0.46%	0.16%	0.21%	0.01%	0.08%
Fraction of intragranular bubbles %		34.6%	46.6%	1.9%	16.9%
$ESD_{50\%}$ (µm)	0.20	0.19	0.20	0.16	0.25
Bubble/m^3	5.42×10^{18}	3.60×10^{18}	1.36×10^{18}	2.77×10^{17}	1.88×10^{17}

Table 4: Intragranular bubble analysis global measurements

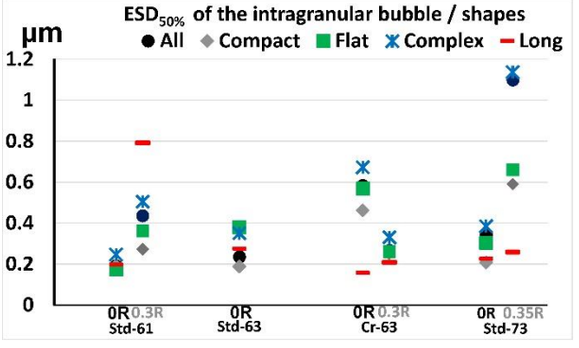

Figure 23: $ESD_{50\%}$ of the intragranular bubbles, according to their shape class

In Figure 24, the histogram graphs give the volume% distribution of the intragranular bubbles as a function of each of their volumes, setting them in *ESD* size classes, for all examined volumes in the central area. The colors in the bars correspond to the shape classification of the bubbles.
Figure 25 provides the same results organized differently to facilitate some inter-sample or inter-position comparisons. The volume% of the bubbles and the bubble densities depending on the shape classes, are

given for all bubbles and for three wider volume classes (*ESD* in 0.038-0.3 µm, 0.3-0.6 µm and above 0.6 µm). These graphs show:

- In the Std-61 sample,
  - More volume made of small compact bubbles at 0R than at 0.3R,
  - Smaller flat and complex bubbles at 0R forming a lower porosity than at 0.3R,
- In the Std-63 sample at 0R,
  - Clearly more small compact bubbles than in the Std-61 at 0R,
  - But also more and larger complex bubbles than in the Std-61 at 0R.
- In the Std-73 sample,
  - At 0R, less small compact bubbles than in the Std-61 at 0R and even less than in the Std-63 sample at 0R,
  - At 0R more complex bubbles than in the Std-61 at 0R and larger ones than in the Std-63 sample at 0R,
  - At 0.35R larger complex bubbles than at 0R in the same sample and than in any other examined position,
- In the Cr-63 sample,
  - Larger and more complex bubbles at 0R than at 0.3R. There is, actually, more compact large bubbles at 0R in this Cr-63 than in the Std-73 at 0R, at a higher burn-up. Yet there is less than in the Std-73 at 0.35R
  - Small and flat bubbles at 0.3R
  - More small compact bubbles than in the Std-61 or the Std-73, but less than in the Std-63.

No particular trend was found for the intragranular long bubbles, on the fringe of flat and complex bubble populations.

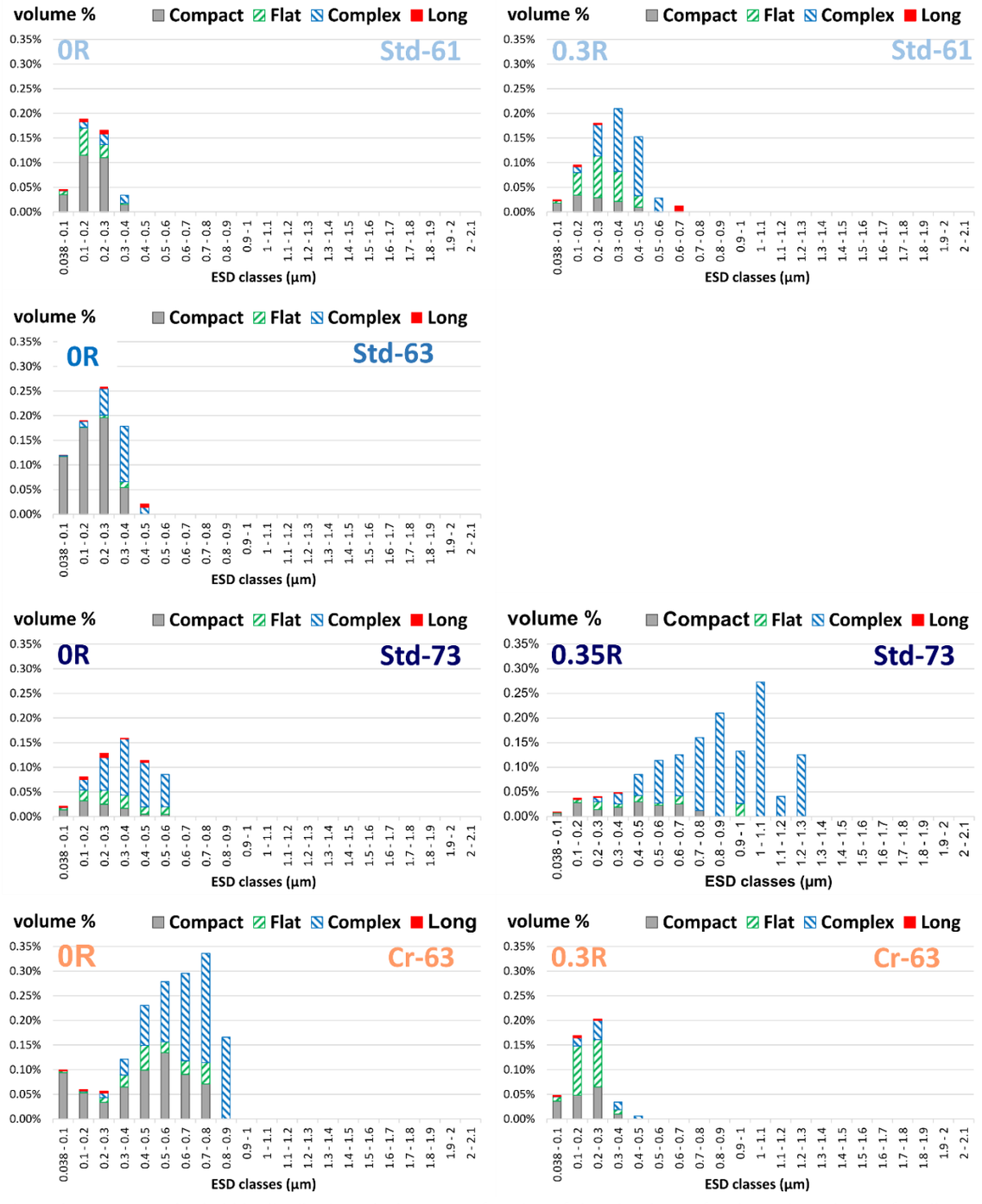

Figure 24: Intragranular bubble distribution, %volume as a function of the ESD classes for the various shapes, for all examined volumes in the central gas precipitation area. The colors in the bars correspond to the shape classification of the bubbles

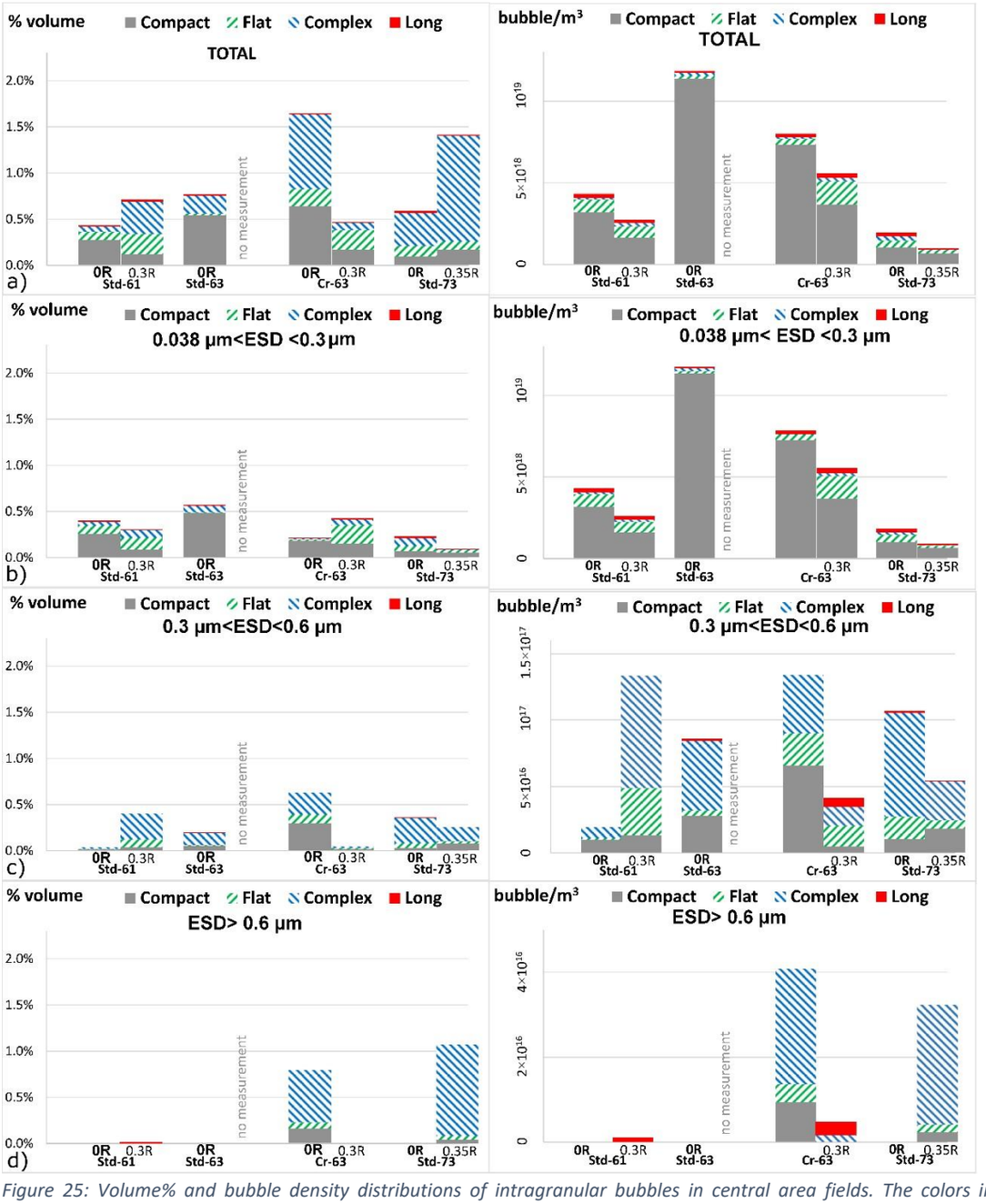

Figure 25: Volume% and bubble density distributions of intragranular bubbles in central area fields. The colors in the bars correspond to the shape classification of the bubbles. Lighter colors are used for the volumes at 0.3R and 0.35R. Each graph gathers results from all examined volumes, a) for all bubbles, b) for bubbles with an ESD between 0.038 and 0.3 µm, c) for bubbles with an ESD between 0.3 and 0.6 µm, d) for bubbles with an ESD higher than 0.6 µm

5. Discussion

In all the high burn-up UO_2 samples examined, in the central areas, some restructuring of the original grains into sub-grains with inter-sub-grain bubbles was found. This applies both to standard UO_2 fuels with ~9 µm grains and to ~60 µm grain Cr doped UO_2 fuels. The sizes of the sub-grains formed were similar for these two types of fuels, around 0.6 µm, despite the initial grain size difference [38].

In these central areas, the general trend found was that the bubbles start as small compact and flat intragranular bubbles. These flat bubbles grow, get thicker and locally interlink, forming larger complex shape bubbles. Despite these growths in bubble size and complexity, no long distance intragranular bubble networks, between these sub-grains, were found. Such networks could have allowed part of the fission gasses to reach the grain boundaries. As mentioned in [57], bubble interconnection might be a reversible process. In these rods submitted to regular nuclear power plant irradiation, the fission gas release fraction increased with the burn-up (as in fig.2 in [33]), so that the general trend was also an increase of the instantaneous release rate. Therefore, there is no period, during these irradiations, for which more interconnected networks than at the end of the irradiation could be expected. If no such network was observed in our samples, none was formed along the irradiation.

In the two Std samples for which two radial positions were studied, the growths in the bubble size and complexity were higher at 0.3R or 0.35R than at 0R.

In the Cr-63 sample, this progress was clearly higher at 0R than at 0.3R. In the Cr-63 sample at 0R, it was also higher than in the two Std samples with a similar burn-up. In this Cr-63 0R case, the growth in bubble size, leading to complex bubbles, also leads to other large bubbles, also with shapes influenced by the surrounding sub-grains, but remaining rather compact. It seems difficult, with these samples only, to attribute these differences to a direct effect of the Cr doping or of the grain sizes. This is all the more difficult that, according to fuel behavior code calculations (Figure 1), the central temperatures in this Cr-63 fuel was slightly lower than that in Std-63 irradiated in the same subassembly. This difference was due to a small enrichment difference (see Table 2) and to a slightly better thermal conductivity due to a slightly higher pellet density at fabrication (lower porosity in Table 2).

Small compact bubbles were found in all samples, but they are clearly more numerous in the Std-63 and Cr-63 0R samples.

In Figure 26 the intragranular fission gas bubble volume%, the complex bubble fractions, the intragranular small flat bubbles and the volume% of small compact bubbles are plotted against the restructuration fraction with angles higher than 1°, in the EBSD study detailed in [38]. This restructuration fraction, in the EBSD maps, is the surface fraction made of sub-grains with an ECD < 3 µm and separated by a continuous boundary with a misorientations higher than 1°.

These graphs show that many of the general trends found in the 3D FIB-SEM bubble characterizations correspond to trends found also in the sub-grain restructuring EBSD characterizations [38]:

- There is a general increase of the porosity and of the fraction of complex bubbles with the progress in the restructuring. This comparison, including all points at 0R and 0.3/0.35R, goes beyond the simple trend of an increase of porosity and of complex bubbles with the burn-up in parallel to the trend of an increase of the restructuring into sub-grains with the burn-up.
- The flat bubble volume%, tends to decrease with the progress of the restructuring. This is the effect of their morphology change into more complex bubbles. The high values found for flat bubbles in the low restructuring situation of the Cr-63 at 0.3R show that even with small misorientations there must have been boundaries formed, but with angles so low that the

sensitivity of our EBSD device, applied on irradiated fuel, cannot detect them. For lower burn-ups, there is no restructuring and no such bubbles. Ranges found for the Cr-63 at 0.3R must, therefore, be seen as a maximum. Nevertheless the lower volume% values found for the Std-61 at 0R correspond, in fact, to a similar high density, but made of smaller flat bubbles.

- In this general trend for the small flat bubbles, the Std-63 0R results stands apart, with low volumes and low densities. This comes with its special position also for the small compact bubbles, with high volumes. It therefore seems that the particularly high presence of small compact bubbles in this fuel at 0R, might have other reasons than the restructuring into sub-grains. It has there to be noted that this sample was taken at a high axial level in this rod and that this rod was located beside a guide thimble, in the subassembly. The high density of small bubbles might be due to local transient at slightly higher powers. In the 3D examination there is, in fact, another sign that this fuel experienced higher temperatures than the other samples studied here. In Figure 27, details of two pores are presented. In addition to the large metallic fission product precipitates, present on the pores' surfaces, particularly where boundaries emerge, other deposits are visible on part of the surfaces. No analyses of these deposits were conducted, but they are likely to be made of volatile fission products. No such deposits were detected in the other samples. Their presence in this sample is likely to be the sign of higher temperatures reached at some point of the irradiation. However, this must have been limited, since no sign of volatile fission product radial or axial migration were detected in the microprobe or gammascanning examinations.

Moreover, in the Cr-63, more locally, the layers around the grain boundaries, showing a low bubble density sample, correspond also, in the EBSD examinations, to un-restructured layers.

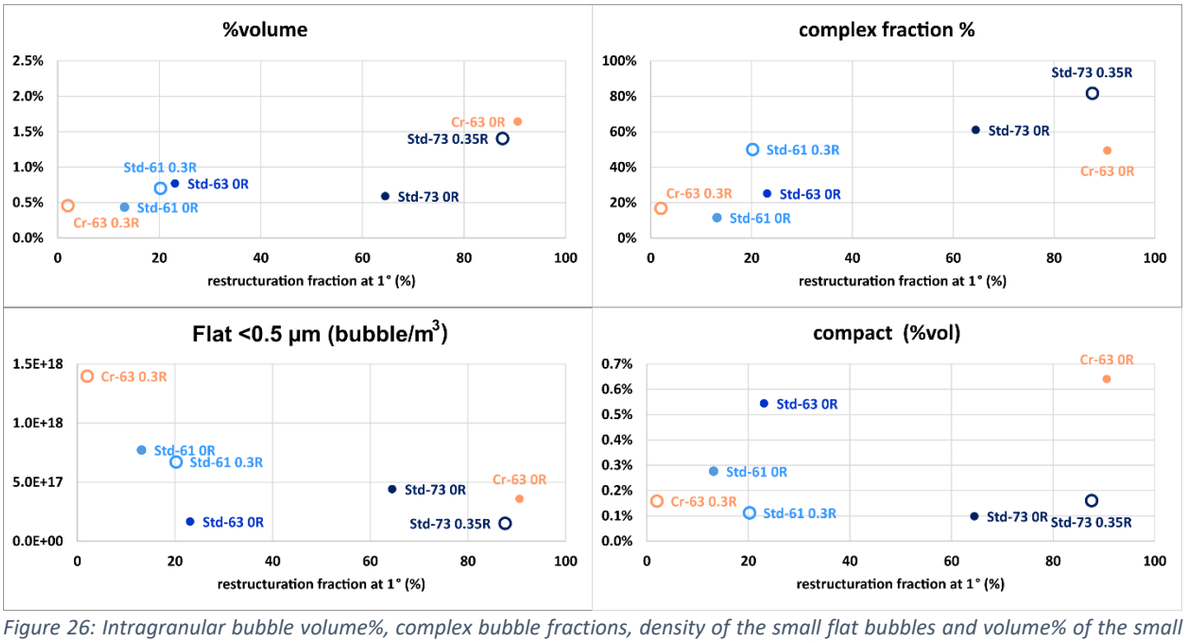

Figure 26: Intragranular bubble volume%, complex bubble fractions, density of the small flat bubbles and volume% of the small compact bubbles, as a function of the restructuration fractions as determined by EBSD [38]

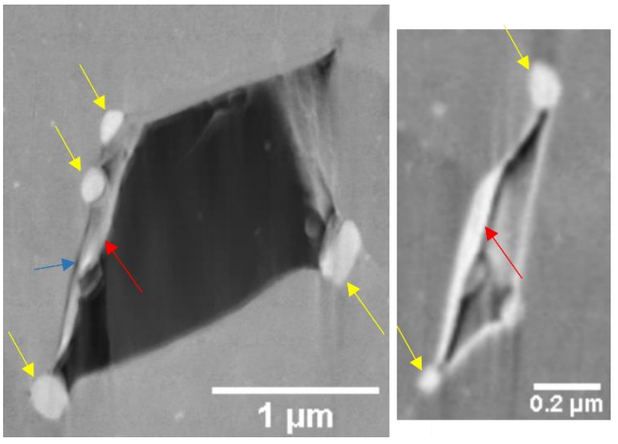

Figure 27: Std-63 at 0R, details on two large bubbles showing the presence of other compound deposits (red and blue arrows) in addition to likely metallic fission products (yellow arrows)

For all Std samples examined, the restructuring and bubble evolutions were therefore more advanced on the periphery of the central area than at 0R. The restructuring was also more advanced on the periphery of the central area than at 0R in the work reported recently by Cappia et al. [36]. An explanation for this trend could be that higher temperatures during the irradiation promoted defect annealing and fission product diffusion in the center thus decreasing the local defect build-up leading to restructuring. Nevertheless, such an explanation leaves a question on the reasons for the often sharp limit between the central area, with bubbles and restructuring, and the intermediate area, at only slightly lower temperatures and very slightly higher burn-up. Moreover, for the Cr-63 sample, the restructuring and bubble evolution was higher at 0R than on the periphery of the central area, and we do not know whether this has directly to do with the Cr doping or with slightly lower temperatures during irradiation. These comments are meant to show that more work is to be done to really address the question about the real reasons for this restructuring and about the real conditions for it to occur and evolve.
Also, in the case reported in [36], the rod had experienced higher linear powers than those reported in this article, leading to a fission gas release fraction of 16%, clearly higher than in our cases. In [36], the bubbles were larger at 0R than on the periphery of the central restructured area. This shows that, higher temperatures, by promoting diffusion, allowed bubble growth. This agrees with the fission gas behavior mechanisms generally considered for that. The bubble growth linked to restructuring is to be viewed as an additional phenomenon that has to be considered, not a phenomenon replacing all mechanisms leading to micrometric fission gas bubbles in the pellet's centers.

On the grain boundaries of the original grains, intergranular bubbles were found. In none of the examined volumes, they formed interconnected networks that could have formed paths for part of the fission gases to reach the grain edges and the rod free volumes. The status of the grain edges however remains unclear. These examinations show the existence of long grain edge bubbles. They also show the existence of discontinuity in these long bubbles. Larger 3D examination volumes would be necessary to precisely know how interconnected these grain edge bubbles can be, in such rods.

The restructuring of the original fuel grains into sub-grains very likely plays a role in the fission gas release fraction increase at high burn-up in rods that never experienced major high linear power periods, as those monitored in [33]. Its existence in the very large grain Cr doped UO_2 has certainly to do with the release fractions found for these very large grain fuel rods. Without being particularly high (see Table 2), the fission gas release fractions found for these fuels imply a higher intragranular transfer towards the grain boundaries than what would be expected for such large grains.

If this restructuring promotes the intragranular to intergranular gas transfer while the 3D FIB-SEM examinations show the absence of interlinked intragranular bubble networks, this means that fission gas diffusion along the low angle boundaries between the sub-grains promotes this transfer. This also means that the trapping into inter-sub-grain bubbles is not high enough to fully prevent this transfer.

In [58] molecular dynamics simulations (MD) showed that Xe atoms diffuse along edge dislocations, but cluster together to form nanometric bubbles. These bubbles incorporate all the isolated mobile Xe atoms thereby inhibiting fast diffusion of Xe along the dislocation core. A similar work examining the fission gas possible diffusion under irradiation, and possible clustering, along low angle boundaries would be necessary to better understand how the gas transfers towards the initial grain boundaries can be promoted by the new microstructure. Such work should include a study of the fission gases resolution outside the bubbles under irradiation, and of the possible effect of a low angle boundary on this resolution. In addition, examinations at higher magnifications, typically transmission electron microscope (TEM) examinations, are necessary for a more complete knowledge of the fission gas status in such microstructures. In particular, parallel to the MD simulations, the presence of nano-bubbles smaller than those accessible by the FIB-SEM examination, along the low angle boundaries seems important to characterize. Such work is ongoing.

These examinations also confirmed, on more samples, what was found in [34] for the Std-73 sample, that no interlinked bubble network forms on the original grain faces during this type of fuel irradiation. Similarly to the situation on the intragranular low angle boundaries discussed above, this means that the increase in the fission gas release at high burn-up implies a diffusion of the fission gasses on the grain boundaries, at least not fully prevented by the trapping in intergranular bubbles whatever their sizes. The observation of a high density of metallic fission product precipitates on the Cr-63 0R grain boundaries, without a similar high density of intergranular fission gas bubbles, Figure 18, seems a good illustration of such a grain boundary long distance atom gas diffusion. For this also, MD simulating grain boundaries and fission gases under irradiation, as well at TEM examinations of these grain boundaries at high magnification would be useful.

6. Conclusion

FIB-SEM 3D examination was conducted on three standard UO_2 PWR fuel samples with grain sizes around 9 µm and average cross section burn-ups between 61 GWd/t_U and 73 GWd/t_U, and one Cr doped UO_2 with grain sizes around 60 µm and a cross section burn-up of 63 GWd/t_U. This work completed other microanalysis examinations, in particular an EBSD work, presented in [38]. Together, they found, in all the central areas of these high burn-up samples:

- a restructuring of the initial grains into smaller sub-grains forming low angle boundaries with crystal orientations around that of their parent grains,
- and intragranular bubbles mostly situated on these low angle boundaries.

The FIB-SEM 3D examination showed how such inter-sub-grain bubbles start as small compact and small lenticular bubbles, similar to typical small intergranular lenticular bubbles. With increasing burn-up, these bubbles grow, get thicker and locally interlink to form larger and more complex bubbles spreading over more than one of these low angle boundaries. No long distance intragranular bubble networks, between the sub-grains, were found. No intergranular bubble interconnected networks were found either. This central restructuring is nevertheless likely to play a role in the increase of the fission gas release fractions at high burn-up. These 3D examinations show that modeling at low scale of the interactions under irradiation, between fission gases and low angle boundaries as well as regular grain boundaries, would be

useful to better understand how part of the gases can leave the grains and the grain boundaries. Higher magnification examinations, such as transmission electron microscopy, are also necessary.
These detailed 3D examinations also evidenced radial differences within each sample and differences between the samples. Many of these differences correspond to differences also found in the degree of restructuring as derived from the EBSD examinations. Nevertheless, these EBSD and FIB-SEM sets of results did not bring a complete understanding in the deep reasons for the measured radial evolutions and the sample to sample differences. In particular, explanations are still lacking for:

- a higher restructuring and bubble evolution on the periphery of the central area than at 0R in the standard UO_2 fuels examined here, but
- with a sharp limit with the intermediate zone,
- whereas for the Cr doped sample, the restructuring and bubble evolution was higher at 0R than on the periphery of the central area, with no outer sharp limit.

This shows that more work is to be done to really address the question on the real reasons for this restructuring and on the real conditions for it to occur and evolve. With an increasing number of high activity laboratories equipped with FIB-SEM and EBSD capacities, a wider set of high burn-up fuels, with more irradiation condition differences, could be available in a near future. It seems worth the effort and the sharing of this type of information.

Conflicts of interest
All authors have no conflicts of interest to declare.

Acknowledgments
The authors are thankful to EDF and FRAMATOME for their support in the studies of these irradiated fuels that they made and used in commercial French nuclear power plants.

[1] L. E. Thomas, in *Fundamental Aspects of Inert Gases in Solids*, edited by S. E. Donnelly and J. H. Evans Plenum, New-York). (1991).

[2] S. Kashibe, K. Une, and K. Nogita, Journal of Nuclear Materials 206 (1), 22 (1993).

[3] J. A. Turnbull, Journal of Nuclear Materials 38 (2), 203 (1971).

[4] M. Mogensen, C. T. Walker, I. L. F. Ray, and M. Coquerelle, Journal of Nuclear Materials 131 (2), 162 (1985).

[5] C. Baker and J. C. Killeen, in *Int. Conf. on Materials for Nuclear Reactor Core Applications, BNES* (Bristol (UK)) (1987).

[6] I. Zacharie, S. Lansiart, P. Combette, M. Trotabas, M. Coster, and M. Groos, Journal of Nuclear Materials 255 (2–3), 92 (1998).

[7] S. Valin, A. Mocellin, G. Eminet, and S. Ravel, in *Fission Gas Behaviour in Water Reactor Fuels*, edited by NEA (OCDE, Cadarache (France)), Vol. NEA #03053, 2002, p. 357 (2000).

[8] R. J. White, Journal of Nuclear Materials 325 (1), 61 (2004).

[9] J. Noirot, C. Gonnier, L. Desgranges, Y. Pontillon, and J. Lamontagne, IAEA-TECDOC-CD-1635, (2009).

[10] M. A. Barker, C. P. Chatwin, and S. L. Owens, in *TOP-FUEL* (Paris (France)) (2009).

[11] J. Noirot, Y. Pontillon, S. Yagnik, and J. A. Turnbull, Journal of Nuclear Materials 462 (0), 77 (2015).

[12] K. Nogita and K. Une, Nuclear Instruments and Methods in Physics Research Section B: Beam Interactions with Materials and Atoms 91 (1), 301 (1994).

[13] K. Nogita and K. Une, Journal of Nuclear Materials 226 (3), 302 (1995).

[14] J. Spino, K. Vennix, and M. Coquerelle, Journal of Nuclear Materials 231 (3), 179 (1996).

[15] H. J. Matzke and J. Spino, Journal of Nuclear Materials 248 (0), 170 (1997).

[16] K. Nogita and K. Une, Journal of Nuclear Materials 250 (2–3), 244 (1997).

[17] M. Kinoshita, T. Kameyama, S. Kitajima, and H. J. Matzke, Journal of Nuclear Materials 252 (1), 71 (1998).

[18] J. Spino, A. D. Stalios, H. Santa Cruz, and D. Baron, Journal of Nuclear Materials 354 (1–3), 66 (2006).

[19] J. Noirot, L. Desgranges, and J. Lamontagne, Journal of Nuclear Materials 372 (2-3), 318 (2008).

[20] D. Baron, M. Kinoshita, P. Thevenin, and R. Largenton, Nuclear Engineering and Technology 41 (2), 199 (2009).

[21] T. Wiss, V. V. Rondinella, R. J. M. Konings, D. Staicu, D. Papaioannou, S. Bremier, P. Pöml, O. Benes, J.-Y. Colle, P. V. Uffelen, A. Schubert, F. Cappia, M. Marchetti, D. Pizzocri, F. Jatuff, W. Goll, T. Sonoda, A. Sasahara, S. Kitajima, and M. Kinoshita, Radiochimica Acta 105 (11), 893 (2017).

[22] F. Cappia, D. Pizzocri, M. Marchetti, A. Schubert, P. Van Uffelen, L. Luzzi, D. Papaioannou, R. Macián-Juan, and V. V. Rondinella, Journal of Nuclear Materials 479, 447 (2016).

[23] F. Cappia, D. Pizzocri, A. Schubert, P. Van Uffelen, G. Paperini, D. Pellottiero, R. Macián-Juan, and V. V. Rondinella, Journal of Nuclear Materials 480, 138 (2016).

[24] T. J. Gerczak, C. M. Parish, P. D. Edmondson, C. Baldwin, and K. A. Terrani, Journal of Nuclear Materials 509, 245 (2018).

[25] J. Noirot, Y. Pontillon, S. Yagnik, J. A. Turnbull, and T. Tverberg, Journal of Nuclear Materials 446 (1–3), 163 (2014).

[26] NEA/CSNI/R(2016)16, (2016).

[27] J. Noirot, T. Blay, J. Lamontagne, L. Fayette, Y. Pontillon, and X. Pujol, in *LOCA Workshop, Fuel fragmentation, relocation and dispersal (FFRD) – experimental basis, mechanisms and modelling approaches* (Aix-en-Provence (France)) (2015) https://hal-cea.archives-ouvertes.fr/cea-01599153.

[28] Y. Yan, J. Harp, K. Linton, and N. Brown, in *TopFuel* (Santander (Spain)) (2021).

[29] T. Narukawa and Y. Udagawa, in *TopFuel* (Santander (Spain)) (2021).

[30] P. Guedeney, M. Trotabas, M. Boschiero, and C. Forat, in *International topical meeting on LWR fuel performance* (Avignon (France)) (1991).

[31] R. Manzel, F. Sontheimer, and R. Würtz, Journal of Nuclear Materials 126 (2), 132 (1984).

[32] J. Noirot, L. Noirot, L. Desgranges, J. Lamontagne, T. Blay, B. Pasquet, and E. Muller, at ANS LWR Fuel Performance, Orlando, Florida (USA), (2004).

[33] J. Noirot, I. Zacharie-Aubrun, L. Desgranges, K. Hanifi, J. Lamontagne, B. Pasquet, C. Valot, P. Blanpain, and H. Cognon, Nuclear Engineering and Technology 41 (n°2), 155 (2009).

[34] J. Noirot, I. Zacharie-Aubrun, and T. Blay, Nuclear Engineering and Technology 50 (2), 259 (2018).

[35] D. Jädernäs, F. Corleoni, A. Puranen, M. Granfors, G. Lysell, P. Tejland, D. Lutz, and L. Hallstadius, in *TopFuel* (Charlotte (NC)) (2013).

[36] F. Cappia, K. Wright, D. Frazer, K. Bawane, B. Kombaiah, W. Williams, S. Finkeldei, F. Teng, J. Giglio, M. N. Cinbiz, B. Hilton, J. Strumpell, R. Daum, K. Yueh, C. Jensen, and D. Wachs, Journal of Nuclear Materials 569, 153881 (2022).

[37] C. McKinney, R. Seibert, G. Helmreich, A. Aitkaliyeva, and K. Terrani, Journal of Nuclear Materials 532, 152053 (2020).

[38] I. Zacharie, R. Dowek, J. Noirot, T. Blay, M. Cabié, and M. Dumont, Journal of Applied Physics (2022).

[39] B. Michel, I. Ramière, I. Viallard, C. Introini, M. Lainet, N. Chauvin, V. Marelle, A. Boulore, T. Helfer, R. Masson, J. Sercombe, J. C. Dumas, L. Noirot, and S. Bernaud, in *Nuclear power plant design and analysis codes* Elsevier, Woodhead Publishing), p. 207. (2020).

[40] V. Marelle, P. Goldbronn, S. Bernaud, E. Castelier, J. Julien, K. Nkonga, L. Noirot, and I. Ramière, in *TOPFUEL* (Boise, Idaho (USA)) (2016).

[41] I. Zacharie-Aubrun, T. Blay, C. Ciszak, C. Cagna, and S. Chalal, in *NuMat* (Montpellier, (France)) (2016).

[42] I. Zacharie-Aubrun and T. Blay, in *Hotlab* (Karlsruhe (Germany)) (2016).

[43] L. Holzer, F. Indutnyi, P. H. Gasser, B. Münch, and M. Wegmann, Journal of Microscopy 216 (1), 84 (2004).

[44] J. R. Wilson, W. Kobsiriphat, R. Mendoza, H.-Y. Chen, J. M. Hiller, D. J. Miller, K. Thornton, P. W. Voorhees, S. B. Adler, and S. A. Barnett, Nature Materials 5 (7), 541 (2006).

[45] J. Schindelin, C. T. Rueden, M. C. Hiner, and K. W. Eliceiri, Molecular Reproduction and Development 82 (7-8), 518 (2015).

[46] C. T. Rueden, J. Schindelin, M. C. Hiner, B. E. DeZonia, A. E. Walter, E. T. Arena, and K. W. Eliceiri, BMC Bioinformatics 18 (1), 529 (2017).

[47] J. Schindelin, I. Arganda-Carreras, E. Frise, V. Kaynig, M. Longair, T. Pietzsch, S. Preibisch, C. Rueden, S. Saalfeld, B. Schmid, J.-Y. Tinevez, D. J. White, V. Hartenstein, K. Eliceiri, P. Tomancak, and A. Cardona, Nature Methods 9 (7), 676 (2012).

[48] K. Li, http://www.cs.cmu.edu/~kangli/code/Image_Stabilizer.html (2008).

[49] B. Münch, L. H. J. Martin, and A. Leemann, Journal of Microscopy 260 (3), 411 (2015).

[50] D. Legland, I. Arganda-Carreras, and P. Andrey, Bioinformatics 32 (22), 3532 (2016).

[51] R. Domander, A. Felder, and M. Doube, Wellcome Open Research 6 (37) (2021).

[52] S. Berg, D. Kutra, T. Kroeger, C. N. Straehle, B. X. Kausler, C. Haubold, M. Schiegg, J. Ales, T. Beier, M. Rudy, K. Eren, J. I. Cervantes, B. Xu, F. Beuttenmueller, A. Wolny, C. Zhang, U. Koethe, F. A. Hamprecht, and A. Kreshuk, Nature Methods 16 (12), 1226 (2019).

[53] R. Kikinis, S. D. Pieper, and K. G. Vosburgh, in *Intraoperative Imaging and Image-Guided Therapy*, edited by Ferenc A. Jolesz Springer New York, New York, NY), p. 277. (2014).

[54] A. Fedorov, R. Beichel, J. Kalpathy-Cramer, J. Finet, J.-C. Fillion-Robin, S. Pujol, C. Bauer, D. Jennings, F. Fennessy, M. Sonka, J. Buatti, S. Aylward, J. V. Miller, S. Pieper, and R. Kikinis, Magn Reson Imaging 30 (9), 1323 (2012).

[55] M. W. Crofton, Philosophical Transactions of the Royal Society of London 158, 181 (1968).

[56] G. Lehmann and D. Legland, The Insight Journal (2012).

[57] J. Rest, M. W. D. Cooper, J. Spino, J. A. Turnbull, P. Van Uffelen, and C. T. Walker, Journal of Nuclear Materials 513, 310 (2019).

[58] S. T. Murphy, P. Fossati, and R. W. Grimes, Journal of Nuclear Materials 466, 634 (2015).

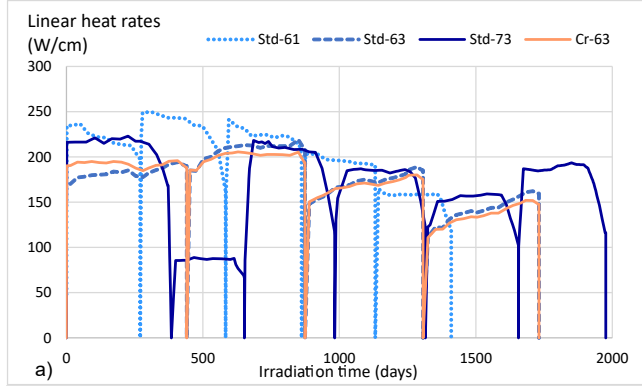
Linear heat rates
(W/cm)
Std-61
Std-63
Std-73
Cr-63
300
250
200
150
100
50
0
0
500
1000
1500
2000
Irradiation time (days)
a)

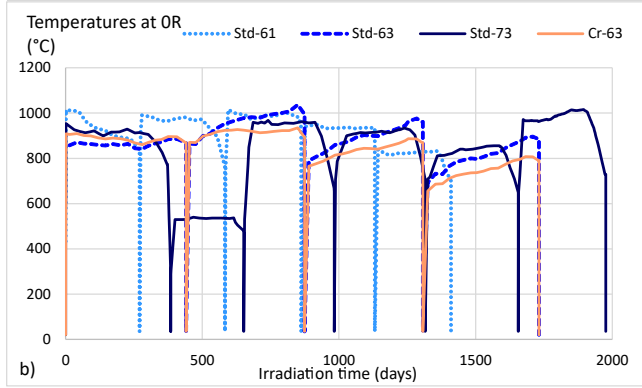
Temperatures at 0R
(°C)
Std-61
Std-63
Std-73
Cr-63
1200
1000
800
600
400
200
0
0
500
1000
1500
2000
Irradiation time (days)
b)

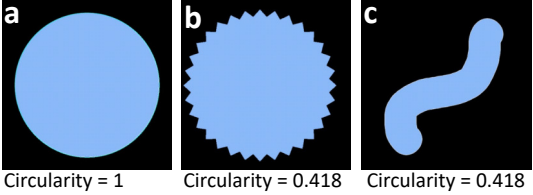
a
b
c
Circularity = 1
Circularity = 0.418
Circularity = 0.418

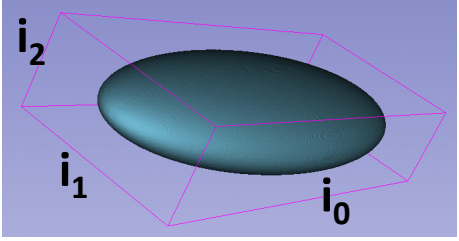
i_2
i_1
i_0

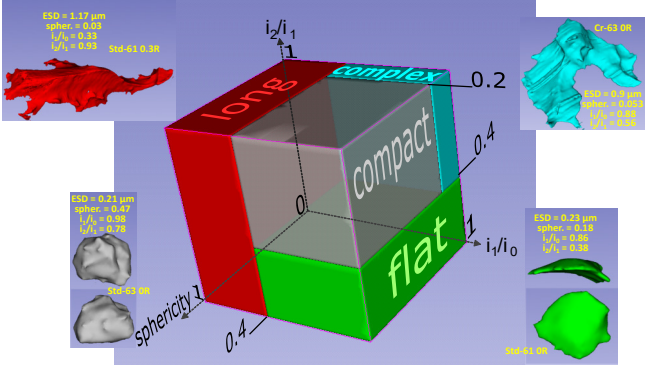
ESD = 1.17 µm
spher. = 0.03
i2/i1 = 0.33
i1/i0 = 0.93
Std-61 0.3R
i2/i1
1
lone
complex
0.2
compact
0.4
0
flat
1
i1/i0
sphericity
1
0.4
Cr-63 0R
ESD = 0.21 µm
spher. = 0.47
i2/i1 = 0.98
i1/i0 = 0.78
Std-61 0R
ESD = 0.23 µm
spher. = 0.18
i2/i1 = 0.86
i1/i0 = 0.38
Std-61 0R

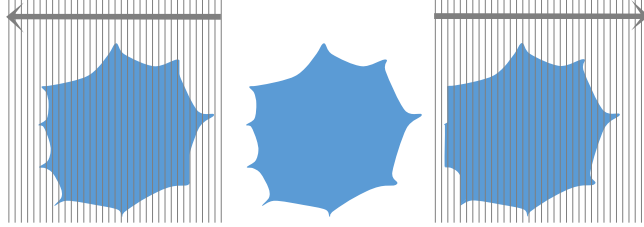

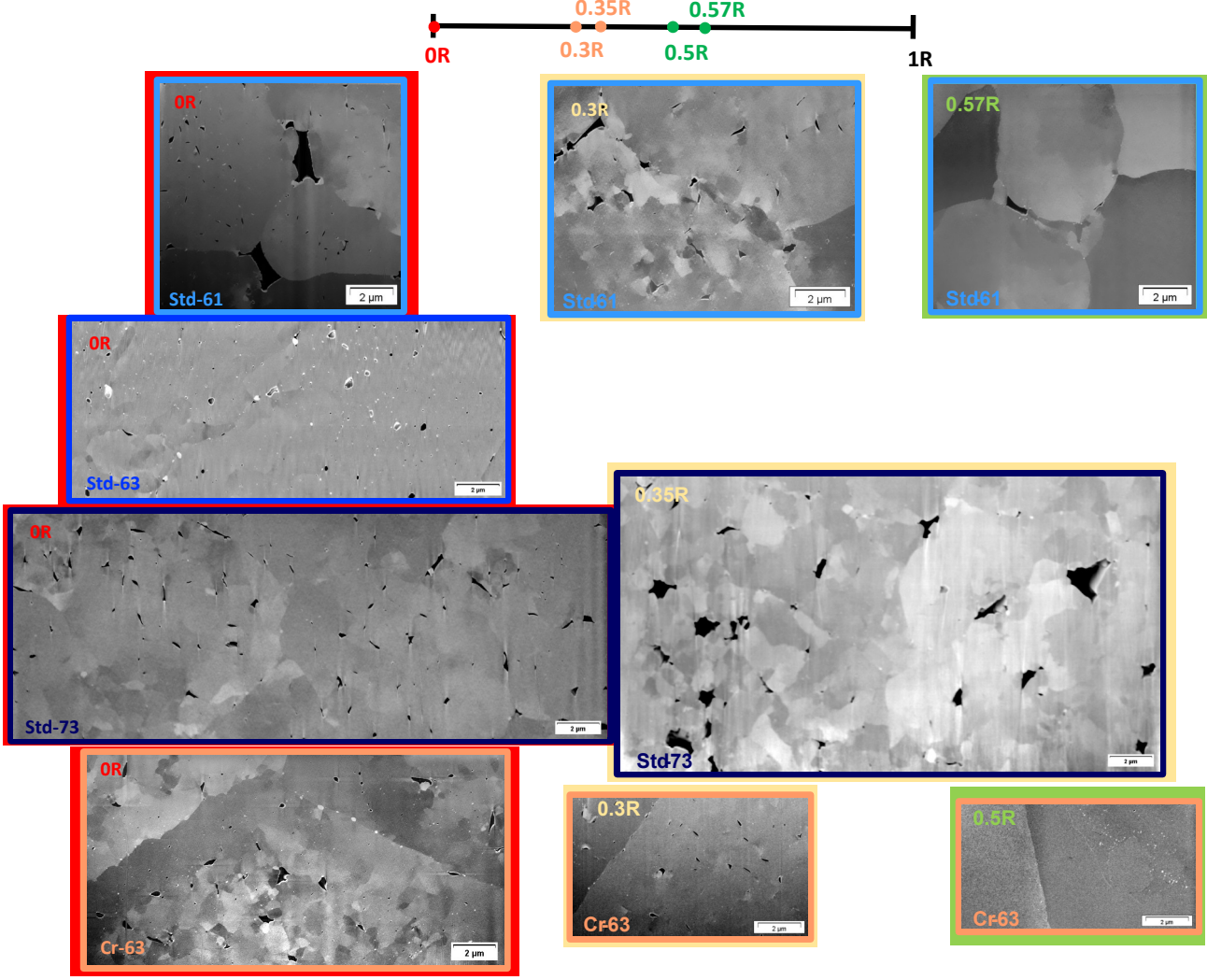
0.35R
0.57R
0R
0.3R
0.5R
1R
0R
Std-61
2 µm
0.3R
Std61
2 µm
0.57R
Std61
2 µm
0R
Std-63
0R
Std-73
0.35R
Std73
0R
Cr-63
2 µm
0.3R
Cr63
0.5R
Cr63

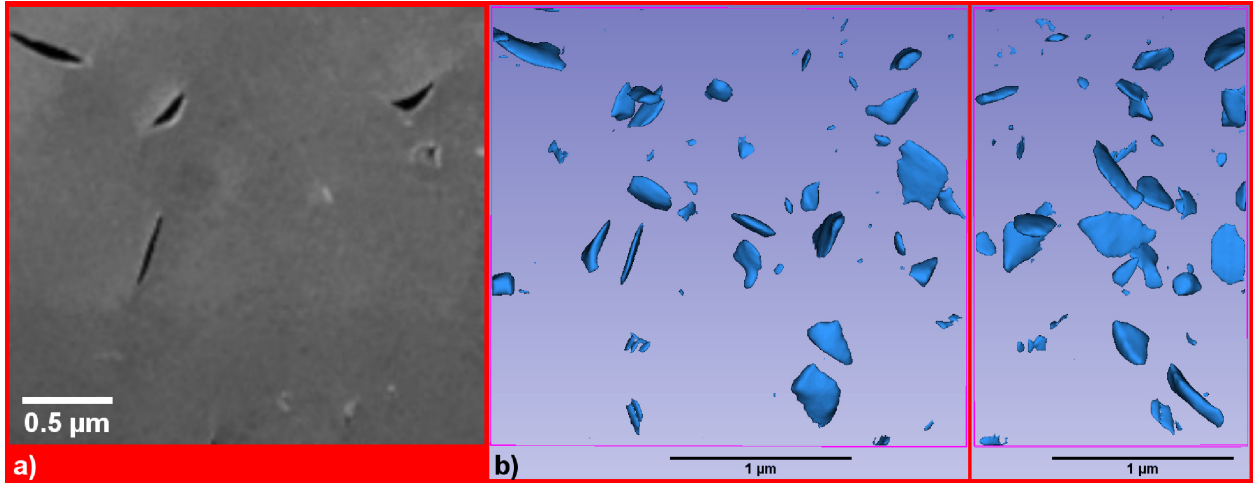
0.5 µm
a)
b)
1 µm
1 µm

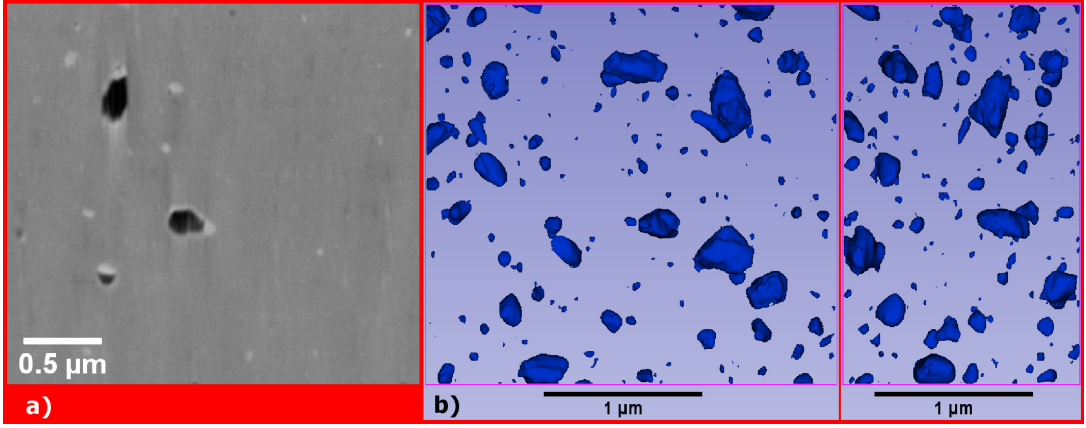
0.5 µm
a)
b)
1 µm
1 µm

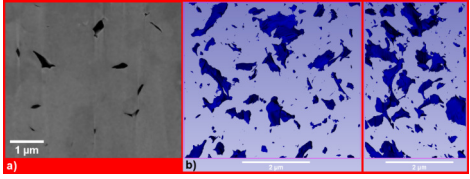
1 µm
a)
b)

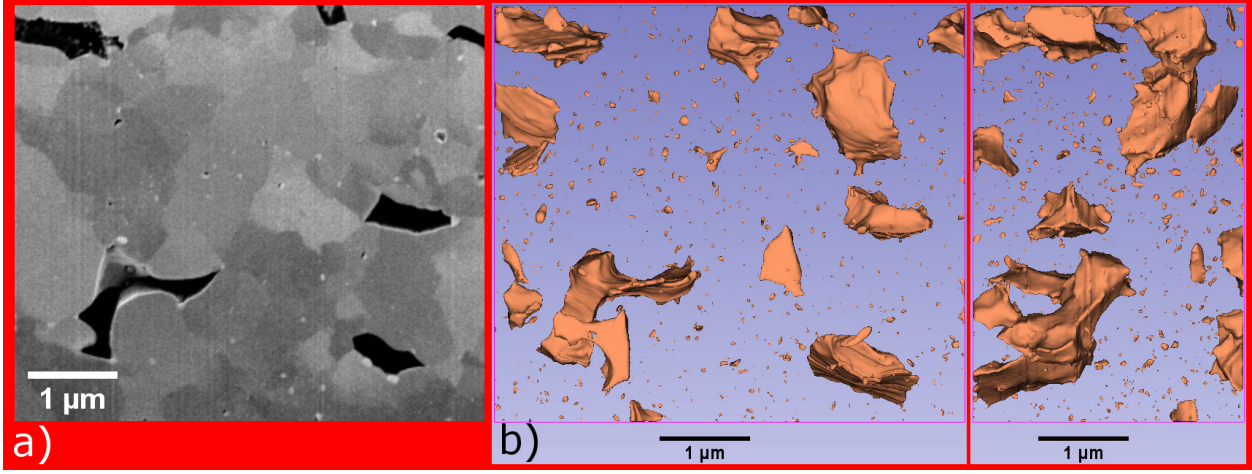
1 µm
a)
b)
1 µm
1 µm

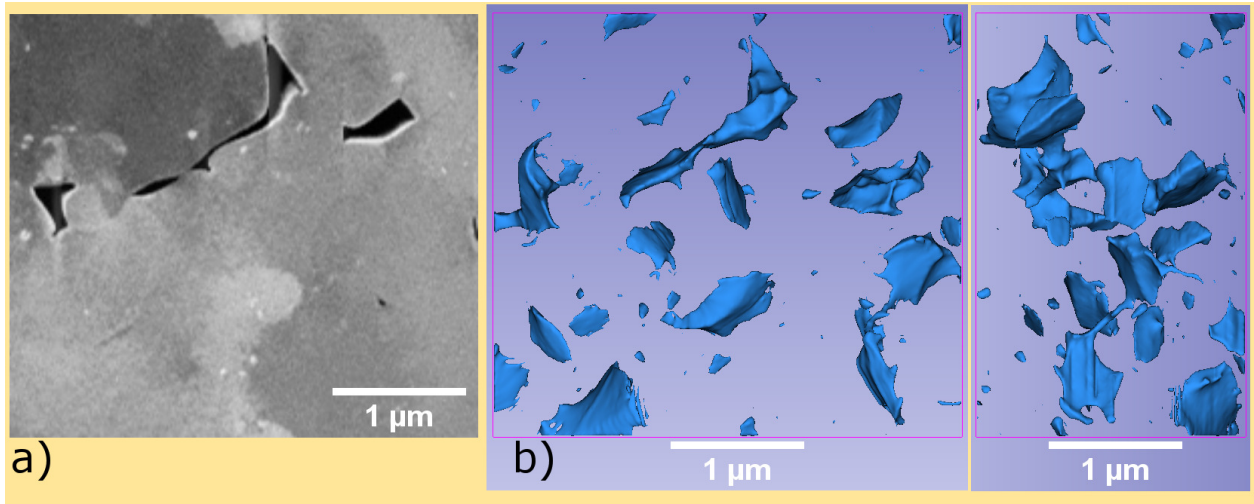
1 µm
a)
b)
1 µm
1 µm

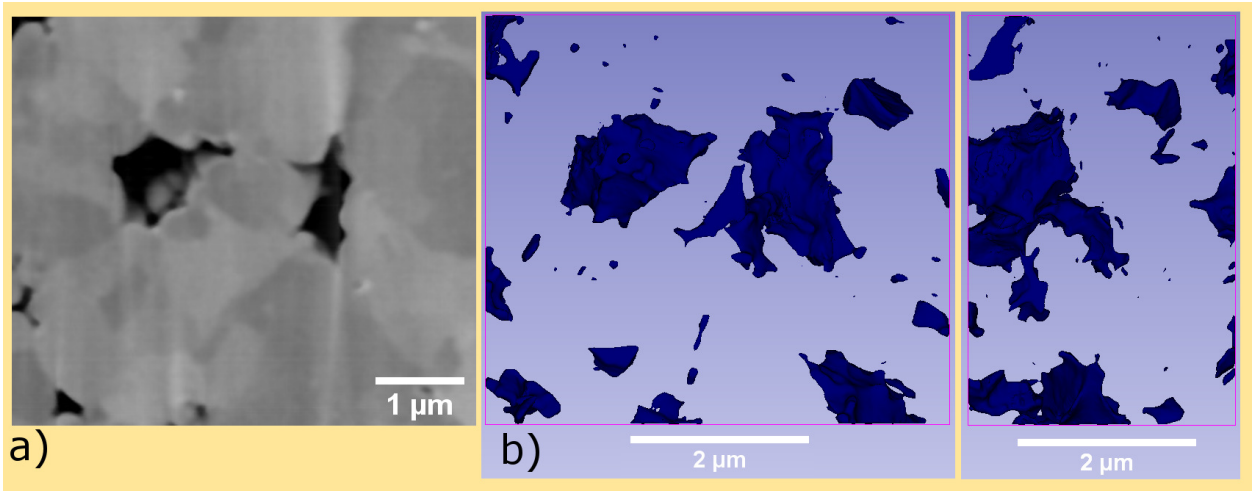
1 µm
a)
b)
2 µm
2 µm

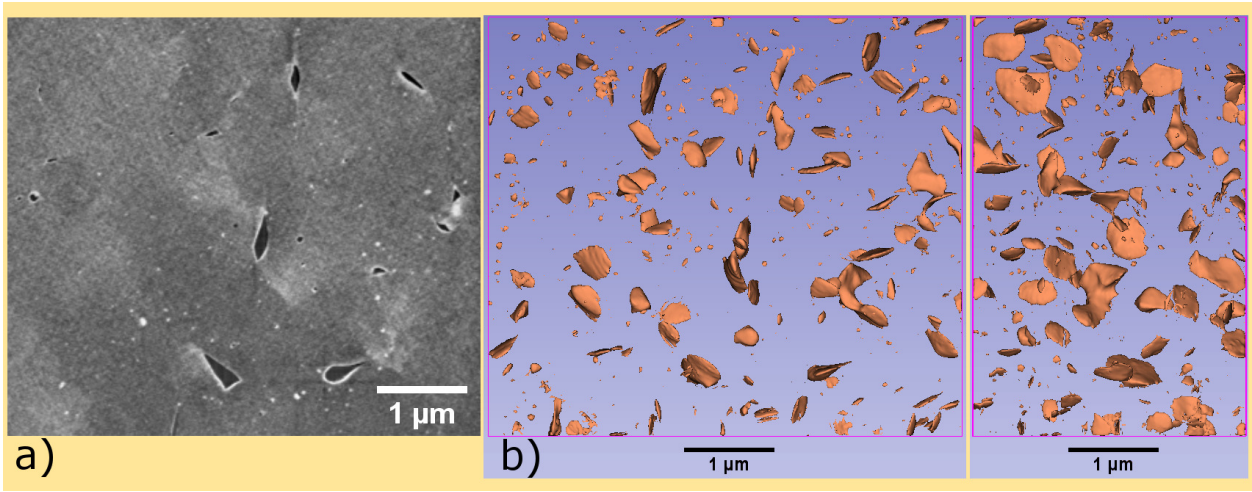
1 µm
a)
b)
1 µm
1 µm

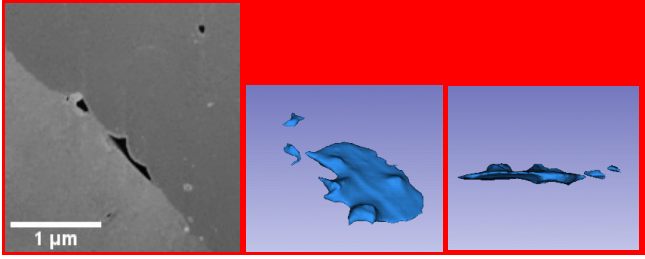
1 µm

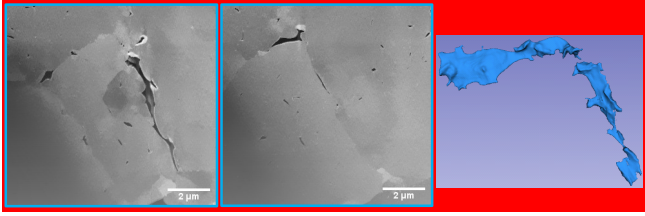
2 µm
2 µm


0.5 µm

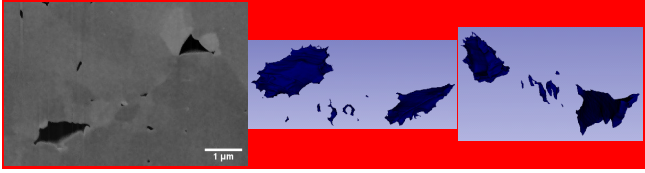
1 µm

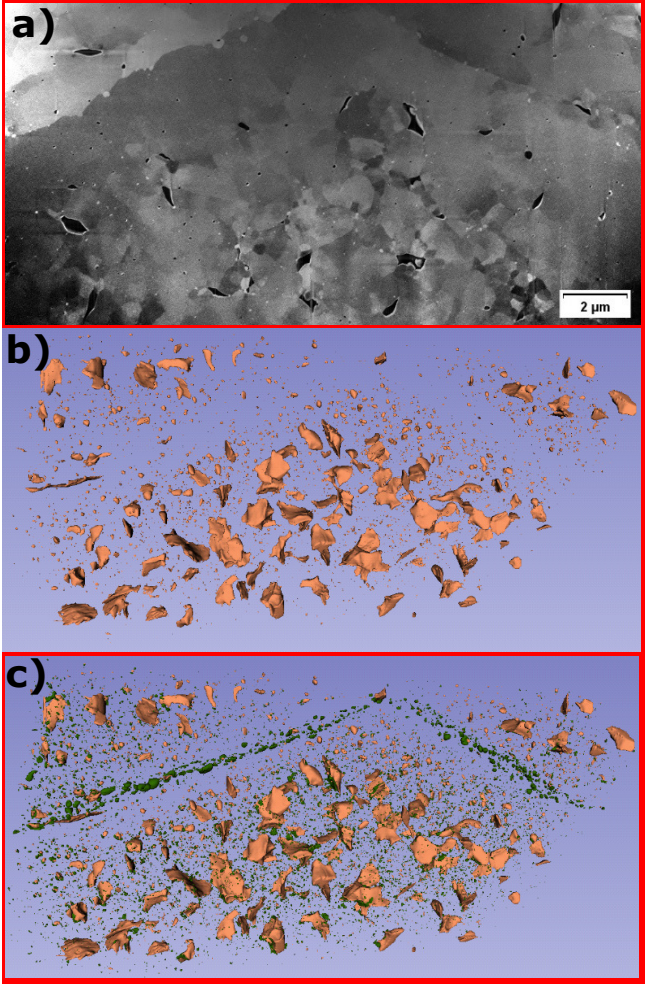
a)
2 µm
b)
c)

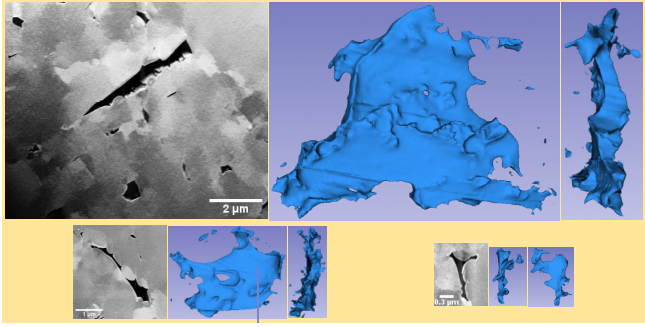
2 µm

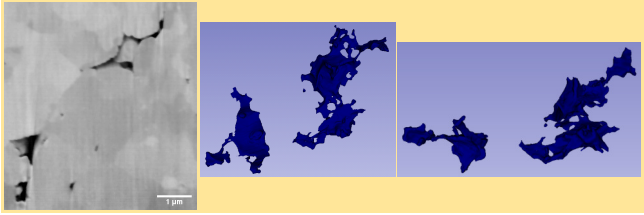
1 µm

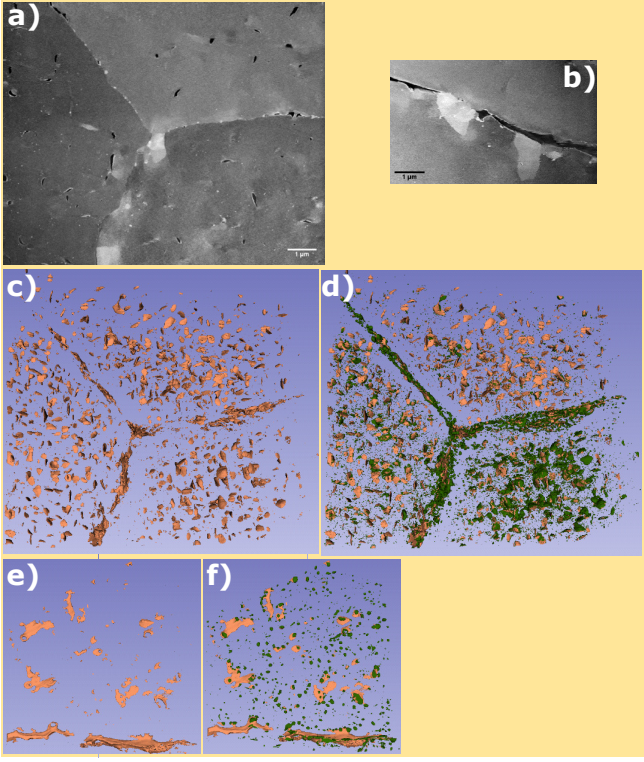
a)
b)
c)
d)
e)
f)

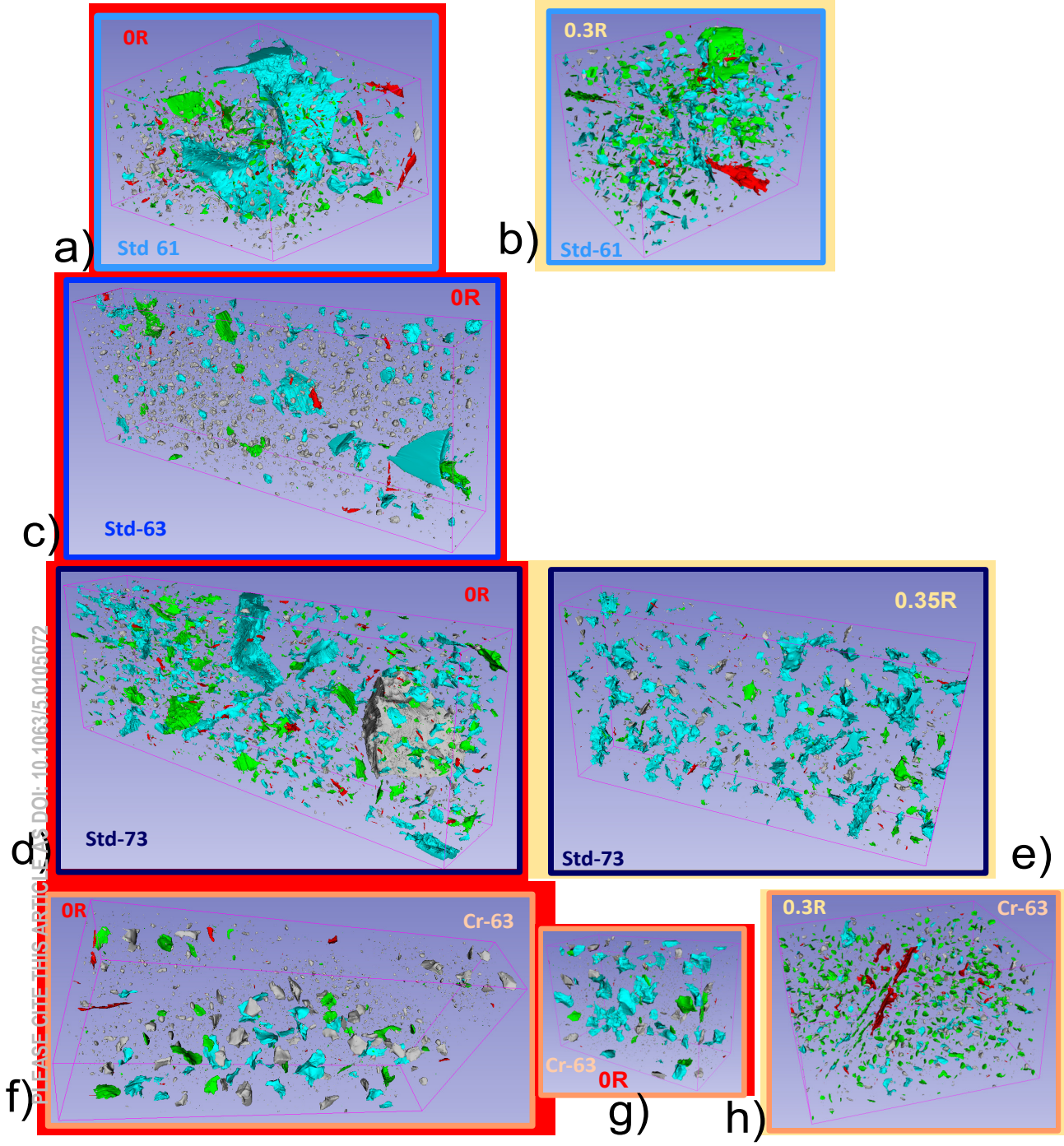

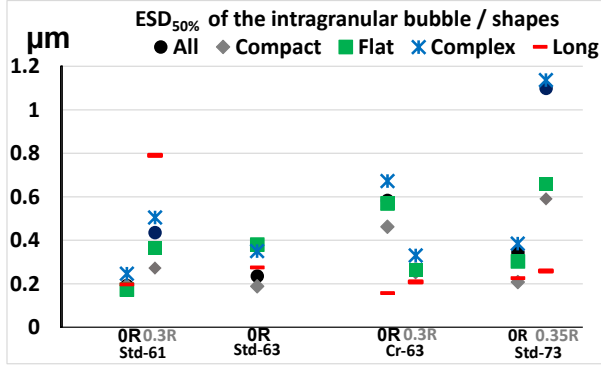
ESD50% of the intragranular bubble / shapes
All
Compact
Flat
Complex
Long
µm
1.2
1
0.8
0.6
0.4
0.2
0
0R 0.3R Std-61
0R Std-63
0R 0.3R Cr-63
0R 0.35R Std-73

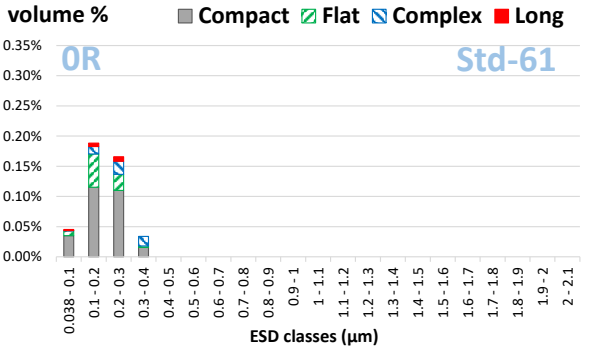
volume %
Compact
Flat
Complex
Long
0R
Std-61
0.35%
0.30%
0.25%
0.20%
0.15%
0.10%
0.05%
0.00%
0.038 - 0.1
0.1 - 0.2
0.2 - 0.3
0.3 - 0.4
0.4 - 0.5
0.5 - 0.6
0.6 - 0.7
0.7 - 0.8
0.8 - 0.9
0.9 - 1
1 - 1.1
1.1 - 1.2
1.2 - 1.3
1.3 - 1.4
1.4 - 1.5
1.5 - 1.6
1.6 - 1.7
1.7 - 1.8
1.8 - 1.9
1.9 - 2
2 - 2.1
ESD classes (µm)

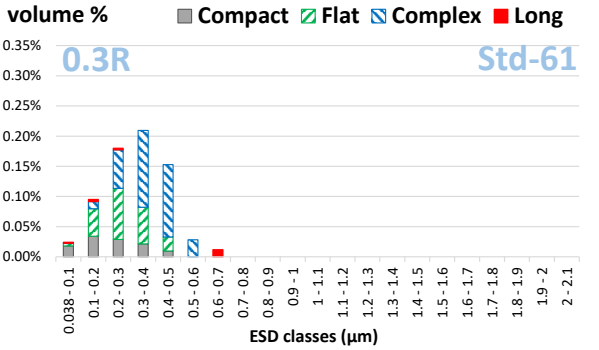
volume %
Compact
Flat
Complex
Long
0.3R
Std-61
0.35%
0.30%
0.25%
0.20%
0.15%
0.10%
0.05%
0.00%
0.038 - 0.1
0.1 - 0.2
0.2 - 0.3
0.3 - 0.4
0.4 - 0.5
0.5 - 0.6
0.6 - 0.7
0.7 - 0.8
0.8 - 0.9
0.9 - 1
1 - 1.1
1.1 - 1.2
1.2 - 1.3
1.3 - 1.4
1.4 - 1.5
1.5 - 1.6
1.6 - 1.7
1.7 - 1.8
1.8 - 1.9
1.9 - 2
2 - 2.1
ESD classes (µm)

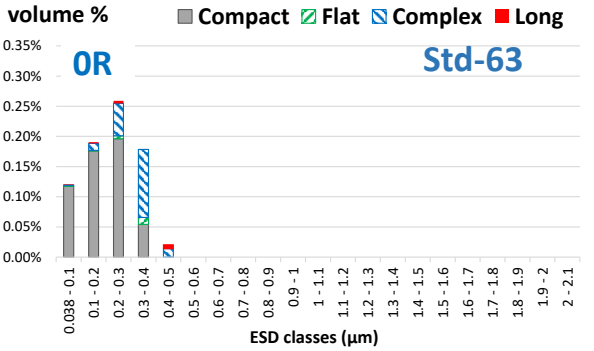
volume %
Compact
Flat
Complex
Long
0R
Std-63
0.35%
0.30%
0.25%
0.20%
0.15%
0.10%
0.05%
0.00%
0.038 - 0.1
0.1 - 0.2
0.2 - 0.3
0.3 - 0.4
0.4 - 0.5
0.5 - 0.6
0.6 - 0.7
0.7 - 0.8
0.8 - 0.9
0.9 - 1
1 - 1.1
1.1 - 1.2
1.2 - 1.3
1.3 - 1.4
1.4 - 1.5
1.5 - 1.6
1.6 - 1.7
1.7 - 1.8
1.8 - 1.9
1.9 - 2
2 - 2.1
ESD classes (µm)

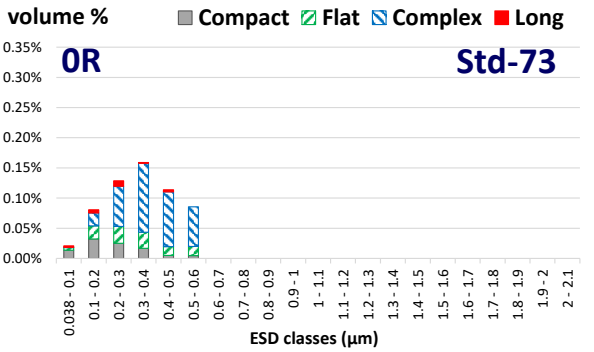
volume %
Compact
Flat
Complex
Long
0R
Std-73
0.35%
0.30%
0.25%
0.20%
0.15%
0.10%
0.05%
0.00%
0.038 - 0.1
0.1 - 0.2
0.2 - 0.3
0.3 - 0.4
0.4 - 0.5
0.5 - 0.6
0.6 - 0.7
0.7 - 0.8
0.8 - 0.9
0.9 - 1
1 - 1.1
1.1 - 1.2
1.2 - 1.3
1.3 - 1.4
1.4 - 1.5
1.5 - 1.6
1.6 - 1.7
1.7 - 1.8
1.8 - 1.9
1.9 - 2
2 - 2.1
ESD classes (µm)

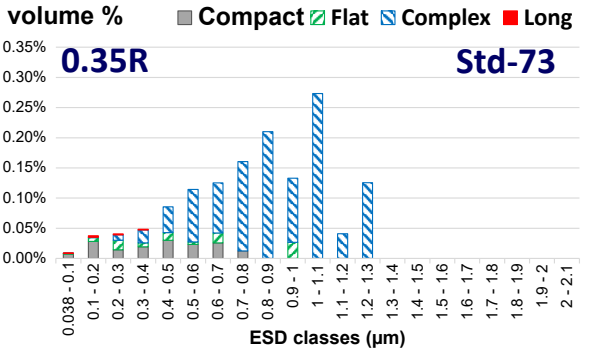
volume %
Compact
Flat
Complex
Long
0.35R
Std-73
0.35%
0.30%
0.25%
0.20%
0.15%
0.10%
0.05%
0.00%
0.038 - 0.1
0.1 - 0.2
0.2 - 0.3
0.3 - 0.4
0.4 - 0.5
0.5 - 0.6
0.6 - 0.7
0.7 - 0.8
0.8 - 0.9
0.9 - 1
1 - 1.1
1.1 - 1.2
1.2 - 1.3
1.3 - 1.4
1.4 - 1.5
1.5 - 1.6
1.6 - 1.7
1.7 - 1.8
1.8 - 1.9
1.9 - 2
2 - 2.1
ESD classes (µm)

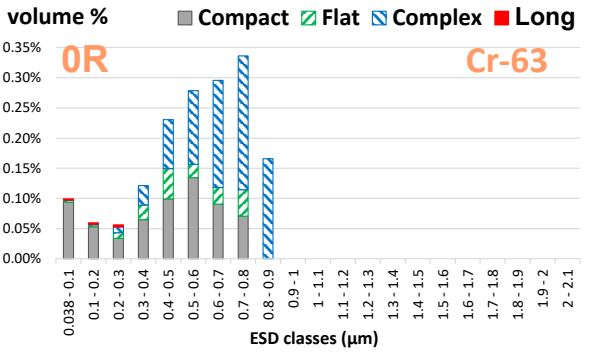
volume %
Compact
Flat
Complex
Long
0R
Cr-63
0.35%
0.30%
0.25%
0.20%
0.15%
0.10%
0.05%
0.00%
0.038 - 0.1
0.1 - 0.2
0.2 - 0.3
0.3 - 0.4
0.4 - 0.5
0.5 - 0.6
0.6 - 0.7
0.7 - 0.8
0.8 - 0.9
0.9 - 1
1 - 1.1
1.1 - 1.2
1.2 - 1.3
1.3 - 1.4
1.4 - 1.5
1.5 - 1.6
1.6 - 1.7
1.7 - 1.8
1.8 - 1.9
1.9 - 2
2 - 2.1
ESD classes (µm)

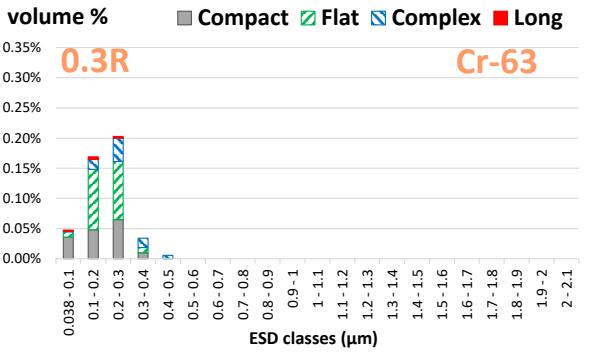
volume %
Compact
Flat
Complex
Long
0.3R
Cr-63
0.35%
0.30%
0.25%
0.20%
0.15%
0.10%
0.05%
0.00%
0.038 - 0.1
0.1 - 0.2
0.2 - 0.3
0.3 - 0.4
0.4 - 0.5
0.5 - 0.6
0.6 - 0.7
0.7 - 0.8
0.8 - 0.9
0.9 - 1
1 - 1.1
1.1 - 1.2
1.2 - 1.3
1.3 - 1.4
1.4 - 1.5
1.5 - 1.6
1.6 - 1.7
1.7 - 1.8
1.8 - 1.9
1.9 - 2
2 - 2.1
ESD classes (µm)

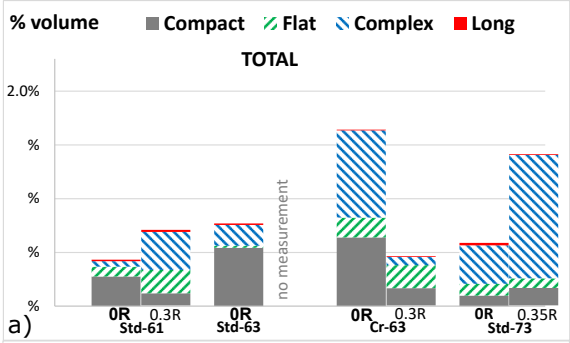
% volume
Compact
Flat
Complex
Long
TOTAL
2.0%
%
%
%
%
%
no measurement
0R 0.3R
Std-61
0R
Std-63
0R 0.3R
Cr-63
0R 0.35R
Std-73
a)

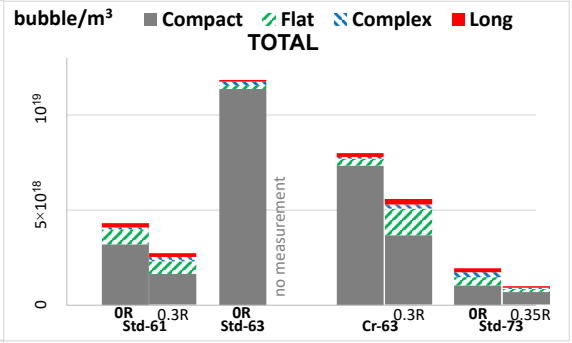
bubble/m³
Compact
Flat
Complex
Long
TOTAL
10¹⁹
5×10¹⁸
0
no measurement
0R 0.3R
Std-61
0R
Std-63
0.3R
Cr-63
0R 0.35R
Std-73

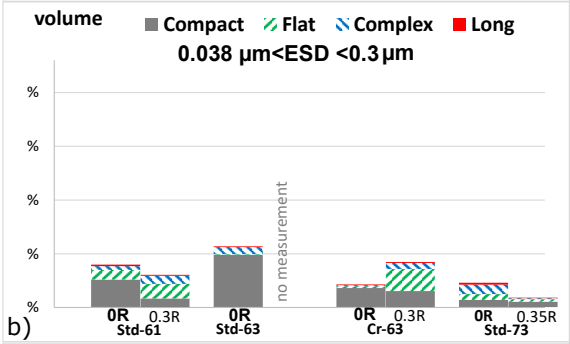
volume
Compact
Flat
Complex
Long
0.038 µm<ESD <0.3 µm
%
%
%
%
%
no measurement
0R 0.3R
Std-61
0R
Std-63
0R 0.3R
Cr-63
0R 0.35R
Std-73
b)

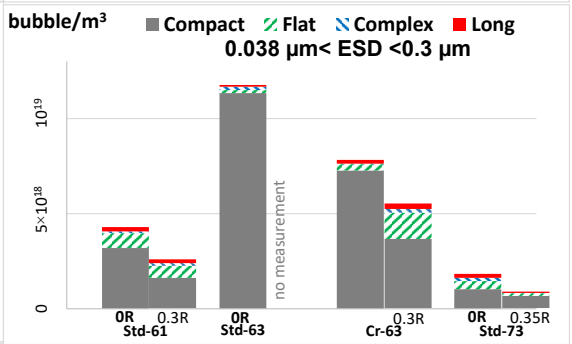
bubble/m³
Compact
Flat
Complex
Long
0.038 µm< ESD <0.3 µm
10¹⁹
5×10¹⁸
0
no measurement
0R 0.3R
Std-61
0R
Std-63
0.3R
Cr-63
0R 0.35R
Std-73

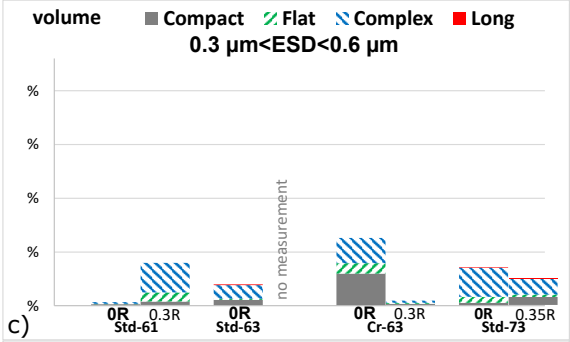
volume
Compact
Flat
Complex
Long
0.3 µm<ESD<0.6 µm
%
%
%
%
%
no measurement
0R 0.3R
Std-61
0R
Std-63
0R 0.3R
Cr-63
0R 0.35R
Std-73
c)

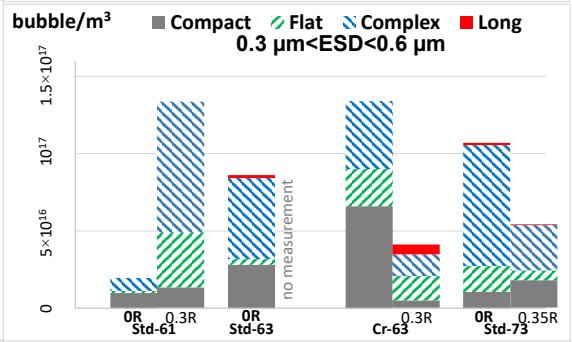
bubble/m³
Compact
Flat
Complex
Long
0.3 µm<ESD<0.6 µm
1.5×10¹⁷
10¹⁷
5×10¹⁶
0
no measurement
0R 0.3R
Std-61
0R
Std-63
0.3R
Cr-63
0R 0.35R
Std-73

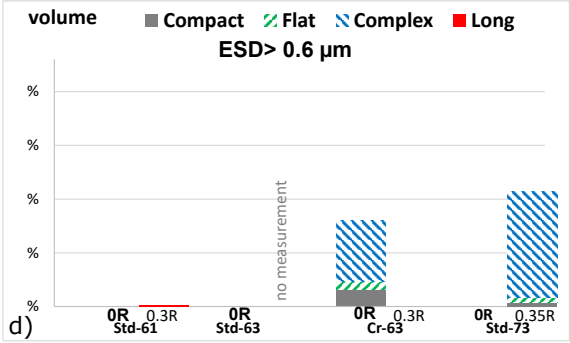
volume
Compact
Flat
Complex
Long
ESD> 0.6 µm
%
%
%
%
%
no measurement
0R 0.3R
Std-61
0R
Std-63
0R 0.3R
Cr-63
0R 0.35R
Std-73
d)

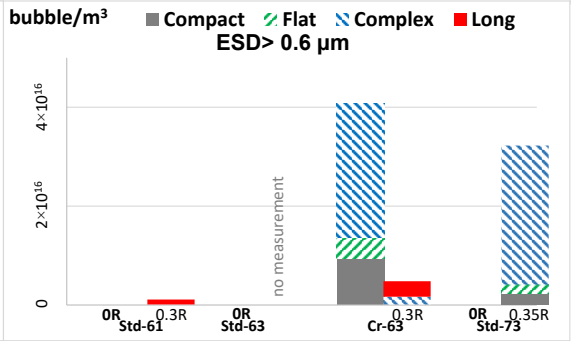
bubble/m³
Compact
Flat
Complex
Long
ESD> 0.6 µm
4×10¹⁶
2×10¹⁶
0
no measurement
0R 0.3R
Std-61
0R
Std-63
0.3R
Cr-63
0R 0.35R
Std-73

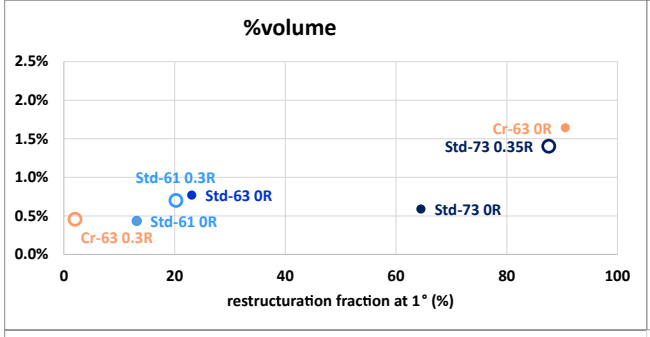
%volume
2.5%
2.0%
1.5%
1.0%
0.5%
0.0%
0
20
40
60
80
100
restructuration fraction at 1° (%)
Cr-63 0R
Std-73 0.35R
Std-61 0.3R
Std-63 0R
Std-73 0R
Std-61 0R
Cr-63 0.3R

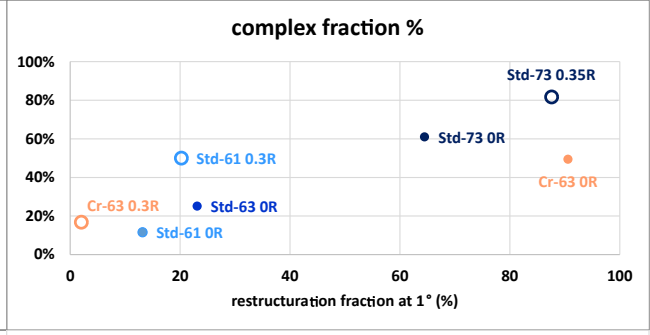
complex fraction %
100%
80%
60%
40%
20%
0%
0
20
40
60
80
100
restructuration fraction at 1° (%)
Std-73 0.35R
Std-73 0R
Std-61 0.3R
Cr-63 0R
Cr-63 0.3R
Std-63 0R
Std-61 0R

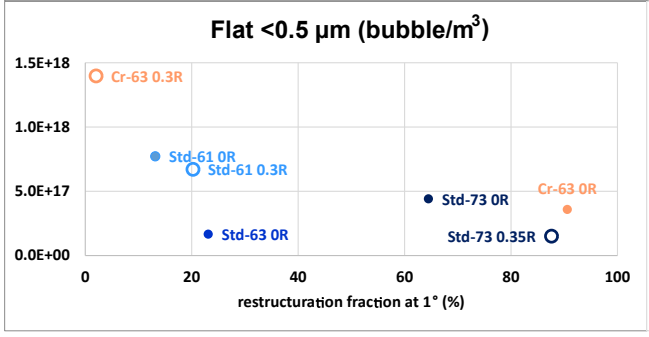
Flat <0.5 µm (bubble/m3)
1.5E+18
1.0E+18
5.0E+17
0.0E+00
0
20
40
60
80
100
restructuration fraction at 1° (%)
Cr-63 0.3R
Std-61 0R
Std-61 0.3R
Std-73 0R
Cr-63 0R
Std-63 0R
Std-73 0.35R

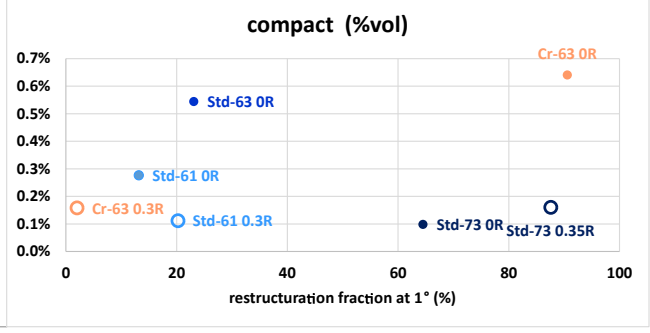
compact (%vol)
0.7%
0.6%
0.5%
0.4%
0.3%
0.2%
0.1%
0.0%
0
20
40
60
80
100
restructuration fraction at 1° (%)
Cr-63 0R
Std-63 0R
Std-61 0R
Cr-63 0.3R
Std-61 0.3R
Std-73 0R
Std-73 0.35R

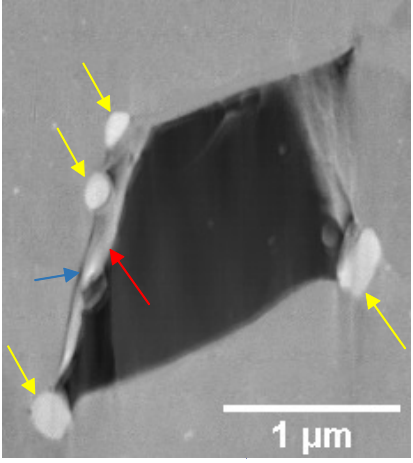
1 µm


0.2 µm